2010

Skeletal Pathology of Tibiotarsi in Chick Embryos Exposed to Platinum Group Metals by Micro-Raman Spectroscopy

Jennifer L. Monahan
Wright State University

SKELETAL PATHOLOGY OF TIBIOTARSI IN CHICK EMBRYOS EXPOSED TO PLATINUM GROUP METALS BY MICRO-RAMAN SPECTROSCOPY

A thesis submitted in partial fullfillment
of the requirements for the degree of
Master of Science

By

JENNIFER LYNN MONAHAN
B.S., Wright State University, 2008

2010
Wright State University

WRIGHT STATE UNIVERSITY

SCHOOL OF GRADUATE STUDIES

June 11, 2010

I HEREBY RECOMMEND THAT THE THESIS PREPARED UNDER MY SUPERVISION BY Jennifer L. Monahan ENTITLED Skeletal Pathology of Tibiotarsi in Chick Embryos Exposed to Platinum Group Metals by Micro-Raman Spectroscopy BE ACCEPTED IN PARTIAL FULFILLMENT OF THE REQUIREMENTS FOR THE DEGREE OF Master of Science .

_____

Ioana Pavel, Ph.D.
Thesis Director

_____

Kenneth Turnbull, Ph.D.
Department Chair

Committee on Final Examination

_____

David Dolson, Ph.D.

_____

Dawn Wooley, Ph.D.

_____

Ioana Pavel, Ph.D.

_____

John A. Bantle, Ph.D.
Vice President for Research and Graduate Studies
Interim Dean, School of Graduate Studies

ABSTRACT

Monahan, Jennifer Lynn. M.S., Department of Chemistry, Wright State University, 2010
Micro-Raman spectroscopy in diagnosing skeletal pathology in chick embryo tibiotarsi exposed to platinum group metals.

Platinum group metals (PGMs) have been shown to accumulate in various tissues of organisms but their toxicity is not well-known. Raman spectroscopy is a powerful analytical technique that enables direct and non-destructive chemical characterization of bone tissues. PGMs were injected into chick embryos in the following concentrations: 0.1, 1.0, 5.0, or 10.0 ppm solutions of $Pt^{(IV)}$, $Rh^{(III)}$, $Pd^{(II)}$ or PGMs mixtures (0.1 ppm or 1.0 ppm of each metal). The micro-Raman maps recorded on the paraffin embedded tibiotarsus cross-sections showed significant changes in the chemical composition and structure of the bone tissue as a result of PGMs exposure of 1 ppm (i.e., anomalous calcium inclusions impeding circulation in cartilage matrix). The following bone properties were analyzed and quantified via micro-Raman spectroscopy: a) age of mineral crystals and carbonate content, b) degree of mineralization of the collagen matrix and possible losses in the organic/inorganic bone components and c) mineral crystallinity. X-Ray fluorescence showed significant changes in the distribution and quantity of calcium and phosphorus due to the PGM treatments. Flame atomic absorption spectroscopy also revealed changes in the amount of calcium found in the tibiotarsi. All three analytical techniques correlated well with each other showing the calcium inclusions negatively affecting the bone structure of the chick embryo tibiotarsi.

TABLE OF CONTENTS

LIST OF FIGURES

LIST OF TABLES

AKNOWLEDGEMENTS

This research could not have been accomplished without the help and guidance of many people. I would like to begin with thanking Dr. Joy Haley, Jon Slagle, Dr. Augustine Urbas and Dr. Tom Cooper for introducing me to physical chemistry research. If it were not for them, I do not know which chemistry career path I would have taken. I would like to thank Dr. David Dolson for recruiting me for the M.S. degree program in Chemistry here at Wright State University. If it were not for his selflessness, I would have never thought about doing research with anyone else. My sincerest thanks go to Dr. Ioana Pavel for her endless guidance and support over these two years. I would not have acquired the knowledge and skills that I have if it were not for her. I would also like to thank Dr. Zofia Gagnon and her students: Brittany NeJame, Jacob Cowley, and David Reens, for beginning this project and Marist College and her vast biological knowledge in aiding in the interpretation of these results. I also would like to acknowledge the guidance of Dr. Dawn Wooley and Dr. David Dolson for being committee members for this research effort. I also appreciate the aid of Lt. Robert Slaughter and Dr. Larry Burgraff with performing the X-Ray fluorescence studies at the Air Force Institute of Technology. My gratitude also goes to our group members: Kent Weaver, Marjorie Makopoulos, Jessica Dagher, Tai Lam, Allie Meyerhoefer, and Khadijeh Alnajjar for their many contributions to this project. Lastly, I would like to thank my family, friends and fellow graduate students for their endless support along this journey.

1. INTRODUCTION

I. BACKGROUND INFORMATION ON PLATINUM GROUP METALS

The platinum group metals (PGMs) class includes the relatively light triad of ruthenium (Ru), rhodium (Rh), and palladium (Pd), and the heavier elements osmium (Os), iridium (Ir), and platinum (Pt). Metallic Os and Ir are not considered biologically important.[1] These metals are found together in sparsely distributed mineral deposits or as by-products when refining other metals.

The development and expansion of vehicles has raised environmental concerns over the past decade. Carbon monoxide, hydrocarbon and nitrogen monoxide emissions from vehicles have been regulated since the 1970s by the use of catalytic converters.[2] Catalytic converters use PGMs to oxidize and reduce these emissions.[3] Pt and Rh reduce nitrous oxides to N_2 and O_2, while Pt and Pd oxidize carbon monixide and hydrocarbons to carbon dioxide.[3] While these metals do aid in reducing the greenhouse gas emissions, they are now at an increased concentration in the environment.[2]

These PGMs are emitted as particulate matter that is considered to be nontoxic.[3] However, PGMs can form complex salts with other compounds (i.e., halogens, cyanides, sulfur, hydroxides) and become biologically active.[2] Therefore, when PGMs are emitted from vehicles traveling along the road, the particulate matter is deposited on the vegetation.[3] If these emissions were to form complex salts, then they can be easily solubilized by rain water and released into various ecosystems.[3] A recent study of automobile emission dust containing Pt, Pd, and Rh particulates found the water soluble

fraction of Pd and Rh to be in the 7.9-13.2 % range, while the water soluble fraction of Pt was below 10%. A higher mobility and bioaccumulation are expected for metal elements that are oxidized to cations in the environment. The higher water soluble fraction for Pd and Rh suggests that those elements could be more available and thus more toxic than Pt to the environment and, subsequently, to human health.[4] In fact, Pt concentrations in a selection of foodstuffs obtained from Australia ranged from 0.13 to 8.1 μg/kg fresh weight.[5] Gagnon *et al*. reported that plant samples collected along roads with only moderate traffic can accumulate high concentrations of PGMs (e.g., an average concentration of 14.6 μg of Pt and 0.75 μg of Rh per g of dry weight tissue).[2,3]

PGMs are introduced into the environment by other means as well, such as from industrial and medical activities. PGMs are used as catalysts in various industrial processes (i.e., ammonia oxidation, reforming crude oil, hydrogenation, etc.). The wastes resulting from these uses enter the ecosystem contain the PGMs in both soluble and insoluble forms.[6] Hospitals and pharmaceutical companies are currently using Pt as an ingredient in various anti-tumor and anti-cancer drugs. A series of investigations initiated by Rosenberg *et al*. to study biological responses to transition metal complexes found that *cis*platinum, *cis*-$[Pt(NH_3)_2Cl_2]$, has antitumor activity.[7] Additionally, certain Pt complexes are effective antitumor agents by producing severe and persistent inhibition of DNA synthesis, as well as the slight inhibition of RNA and protein synthesis.[1]

Once PGMs enter the ecosystems, they have been shown to bioaccumulate in various tissues, both plant and animal. This provides a potential for adverse effects on various living organisms, including humans. In general, the environmental impact, toxicity, and bioavailability of these heavy metals in living organisms remain unclear.[6]

PGM accumulation through dietary intake in animal models such as earthworms[8] and rats[9] has also been documented. The accumulation of PGMs resulted in pathological and genotoxic responses in all models. The consequential exposure to PGMs in animals showed changes in adrenal glands, glomeruli of the kidney, and white pulp of the spleen, while plants exhibited growth inhibition. Humans may be exposed to PGMs by ingestion through dietary intake or by inhalation of the particulate matter. However, there have only been a few studies to assess this threat to human health.[10] These few studies showed exposures to PGM emissions cause disease-like symptoms including asthma, miscarriages, allergic reactions, nausea, loss of hair, and mucous membrane irritations.[3,6] Additionally, Pt was found to be the most toxic PGM toward organisms due to its high affinity to bind to proteins. The World Health Organization showed in 2002 that PGM compounds might cause severe respiratory conjunctivitis.[11]

EXPERIMENTAL DESCRIPTION

The proposed experiment will inject developing White Leghorn strain chick embryos with Pt, Rh, Pd, and a mixture of the three metals as a salt solution. Injections will be made on the 7^{th} and 14^{th} days of incubation and the embryos will be sacrificed on the 20^{th} day. Various organs will be harvested and in particular, the tibiotarus will be fixed, embedded, sliced, and placed on a microscope slide. The tibiotarsus was chosed for examination via micro-Raman spectroscopy due to the ease of accessibility of this bone for harvesting. Micro-Raman spectroscopy was utilized in order to study the morphology and chemical content within the tibiotarsus cross-section. Further studies using X-Ray fluorescence microscopy and flame atomic absorption spectroscopy were used to confirm the information gained from the micro-Raman analysis.

PRELIMINARY RESULTS

Our preliminary experiments exposed developing chick embryos to a single-element injection of 5.0 ppm Rh. This exposure revealed the formation of calcium deposits in the brain tissues of developing chick embryos (Figure 1.1). The mechanism for this response is unknown. In addition, all embryos surviving the sub lethal dose of 5.0 ppm Rh experienced incomplete development of rib cages and/or skulls. Therefore, this project will focus on the skeletal pathology of tibiotarsi, a model for bone development, in developing chick embryos exposed to PGMs by micro-Raman spectroscopy and other complimentary techniques.

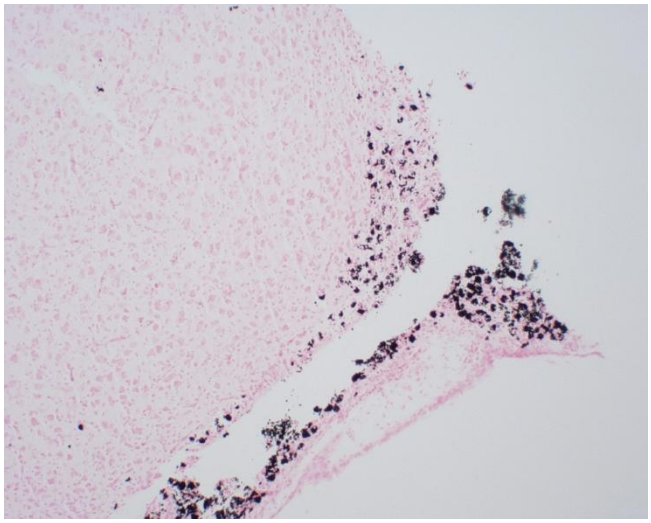

Figure 1.1: Calcium deposits (black spots) observed in the brain tissue of developing chick embryos treated with 5.0 ppm of Rh. The slide was stained using the Von Kossa protocol.

HYPOTHESIS

It is hypothesized that PGMs may penetrate the cartilage tissue in developing chick embryos and interfere with calcium metabolism in this tissue.

SCIENTIFIC AIMS

1. To show that abnormal calcium inclusions and/or calcium redistribution occur within the cartilage tissue cross-sections when exposed to PGMs above a specific threshold level.

2. To show that PGM exposure levels correlate negatively with calcium content and morphology in the tibiotarsi of developing chick embryos.

II. CHICK EMBRYO CARTILAGE COMPOSITION AND MORPHOLOGY

CARTILAGE

The avian model resembles other amniotes, including mammals, in some characteristics of skeletal development.[12] The embryonal skeleton is initially formed as cartilage, which ultimately becomes ossified.[13] The cartilage is an essential first step to development and growth of long bones.[13] However, the cartilage growth plates disappear when postnatal growth is over. Cartilage has *no capillary blood supply (avascular)* of its own so its cells must obtain oxygen and nutrients by *long-range diffusion*. The cartilaginous matrix is a resilient gel-like structure with specific macromolecular organization. Tissue fluids partially trap and bind matrix constituents, and account for 65% to 80% of the wet weight of the matrix. The major volume of tissue fluid in the matrix facilitates long-range diffusion of oxygen and nutrients to chondrocytes from capillaries that lie outside the cartilage. The long-range diffusion process is essential in gas exchange and waste removal. Metabolic byproducts of the cartilage tissue follow a reverse diffusion path to these outside capillaries. Dependence on this long diffusion pathway is hazardous, especially if matrix proteoglycans become displaced by insoluble calcium salt inclusions.[13]

The embryonic cartilage cells differentiating at the sites of developing cartilages are called chondroblasts. These cells are responsible for secreting the macromolecular constituents of the cartilage matrix. Chondroblasts at the periphery of these sites form a fibrous covering known as perichondrium. The outer perichondric cells differentiate into fibroblasts, which produce collagen. This fibrous outer layer of the perichondrium remains in adult life with a few exceptions. For example, articular cartilages are devoid of perichondrium. The inner part of the perichondric covering is responsible for chondrogenesis, i.e., the cartilage development. The chondrogenic cover continuously creates new chondroblasts that built up the collagen matrix. Chondroblasts buried in the cartilage matrix are described as chondrocytes. Chondrocytes are enclosed in tiny matrix compartments known as lacunae. Each living chondrocyte virtually fills its lacuna. Chondrocytes are metabolically very active and essential in the synthesis of numerous matrix components.[8] Mature chondrocytes are large secretary cells with a spherical nucleus and a prominent nucleolus. Initially their cytoplasm is basophilic, but later it contains numerous fat droplets and appears vacuolated.[13]

The cartilage tissue may grow simultaneously in two different ways: interstitial and appositional. Interstitial growth is characteristic to the cartilage alone and cannot occur in bone. According to this growth mechanism, the cartilage expands because of the increase in the population of proliferative chondrocytes and accompanying supplementary matrix production. Appositional growth may be observed in both cartilages and bones. According to this growth mechanism, the cartilage expands due to the increase in the number of chondroblasts from the perichondrium and the

incorporation of new supplementary matrix constituents that they produce at the outer layer of the cartilage.[13]

Collagen accounts for 40% to 70% of the dry weight of the cartilage matrix and is constituted by abundant type I and type II collagen fibers. Conspicuous parallel bundles of type I collagen fibers form the fibrocartilage, which resist stretching under extreme tension. Fibrocartilage is avascular.[8] Fine type II collagen fibers together with acidophilic elastic fibers make up the elastic cartilage, which is adapted to withstand repetitive bending.[13]

BONE

Cartilage that undergoes endochondral ossification (i.e., an ossification process characteristic to long bones) is replaced by bone. In embryonal development, the tibiotarus is completely formed by day five and ossification occurs shortly thereafter. The ossification process is completed eleven weeks after hatching. Similar to formation of the limb skeleton, the skull begins to ossify by day nine of incubation. By the forteenth day of incubation, most of the skull bones have undergone ossification. During the later stages of development, the embryo obtains its calcium from the egg shell.[13]

Four bone cell types: osteogenic stem cells (osteoprogenitors), bone matrix producers (osteoblasts), bone matrix maintaining cells (osteocytes), and bone matrix-resorbing cells (osteoclasts) are present in the chick embryo. Osteoprogenitor cells, which are stimulated to proliferate, create osteoblasts in regions that are well vascularized. Osteoblasts are specialized nondiving cells that synthesize and secrete the organic constituents of the bone matrix. These cells are also implicated in the process of matrix calcification and have an additional role of mediating the bone resorption. The

development of osteocytes represent the final stage of maturation of the bone cell lineage and their function is to maintain the bone matrix in good repair. Osteoclasts are large nondividing motile cells that help remodeling the bone by resorbing surplus or inferior bone matrix.[13]

Similar to the cartilage tissue, the bone tissue contains living cells embedded in an extracellular matrix that is reinforced by collagen fibrilis. Like chondrocytes, the cells embedded in the bone matrix, known as osteocytes, occupy lacunae. Another similar feature is the presence of a fibrous connective tissue covering called *periosteum*, which is the counterpart of perichondrium.[13]

However, in contrast to the cartilage matrix, the bone matrix is heavily calcified and is constantly replaced throughout the bone remodeling or turnover process.[14] This makes the bone harder and less supple than the cartilage. Bone matrix withstands bending, twisting, compression, and stretch. These mechanical properties provide the structural support and mobility of the avian body and offers protection of vital organs. Additionally, osteocytes differentiate in regions close to *capillaries* (i.e., 0.2 mm radius of a capillary), while chondrocytes are essentially devoid of blood vessels. Therefore, a clear difference is expected in the way the two types of cells nourish since the high bone mineral content severely limits the *long-range diffusion* through the tissue.[13]

Osteocytes survive in the hostile stone-like bone matrix due to the presence of canaliculi and the highly vascularized tissue. These canals interconnect the lacunae with one another and link them to the bone surfaces that are bathed by tissue fluid. Canaliculi bring tissue fluid, oxygen, and nutrients to all osteocytes. Additionally, the tissue fluid

produced by blood capillaries reaches the surrounding osteocyte cells by way of the canaliculi.[13]

Almost 70% of the wet weight of the bone matrix is bone mineral, primarily represented by hydroxyapatite. The insoluble calcium salts make the bone rock-hard. Only 25 % of the bone tissue is water. More than 90% of the organic content of the bone matrix is given by type I collagen together with small amounts of type V collagen (i.e., a higher percentage than in the cartilage matrix). Due to higher abundance of collagen fibrils, the bone matrix is highly resistant to tensile stresses. Other organic constituents of the bone matrix are glycosaminoglycans, glycoproteins, osteonectin (i.e., a protein that anchors bone mineral to collagen), osteocalcin (i.e., a calcium-binding protein), and other matrix proteins that have the capacity to induce bone formation.[13]

III. CHICK EMBRYO MODEL

The chick embryo model has been embraced due to its notable history in various biological studies (i.e., immunology, genetics, cell biology, embryology, virology, and developmental biology).[15,16] This model has been studied since the time of the ancient Egyptians and Aristotle in order to understand the development of the chick embryo.[16] By the end of the 19th century, scientists began manipulating the chick embryos in order to understand the developmental potential of the cells.[16] This led to detailed fate maps, formal definition of important concepts, and to the general conclusion that development depends on the flow of instructive signals between the different cells.[16] During the mid 20th century, scientists became more interested in the human, fly, frog, and mouse genome due to the discovery of gene expression, and the chick embryo model lost momentum.[16] In the late 20th century, another resurgence of the chick embryo model

arose due to many technological advances in stem cells and genomics research.[16] By 2005, the chicken genome sequence was complete and became a popular model system.[15] The National Institute of Health (NIH) has recently recognized the chick embryo as a readily available and well-developed biological model for pharmaceutical and toxicological studies.[17]

The chick embryo model was employed in this study due to the well-established and inexpensive experimental methods associated with it in comparison to other animal models.[17] During chick development, the permeability of the blood-brain barrier changes during the 21-day gestation cycle.[18] Figure 1.2 shows Hamburger and Hamilton's (HH) stage 30 and 40[19] of the developing chick embryo. At stage 30, the segments of the wings are clearly seen and bent at the elbow joint.[19] The legs are bent and the webs between the toes are slightly curved.[19] The mandibular process is beginning to approach the beak but the gap is still noticeable.[19] The neck has also lengthened drastically between the collar and the madible.[19] The beak may also be seen but is not fully developed.[19] At stage 40, the length of the beak is 4.0 mm and the length of the third toe is 12.7 ± 0.5 mm, which are important characteristics for the chick to begin hatching.[19] The formations of scales on the inferior and superior surfaces of the legs are also noticeable. The foot is also covered with well-developed papillae.[19] In this study, embryos were injected with various PGM treatment solutions during these stages. This allowed the chick embryos to mature with a new treatment medium in place. Chick embryos develop rapidly and are easily accessible at all stages.[11] Lastly, the embryos are not considered vertebrate animals before hatching. Therefore, no special animal license is required.[11]

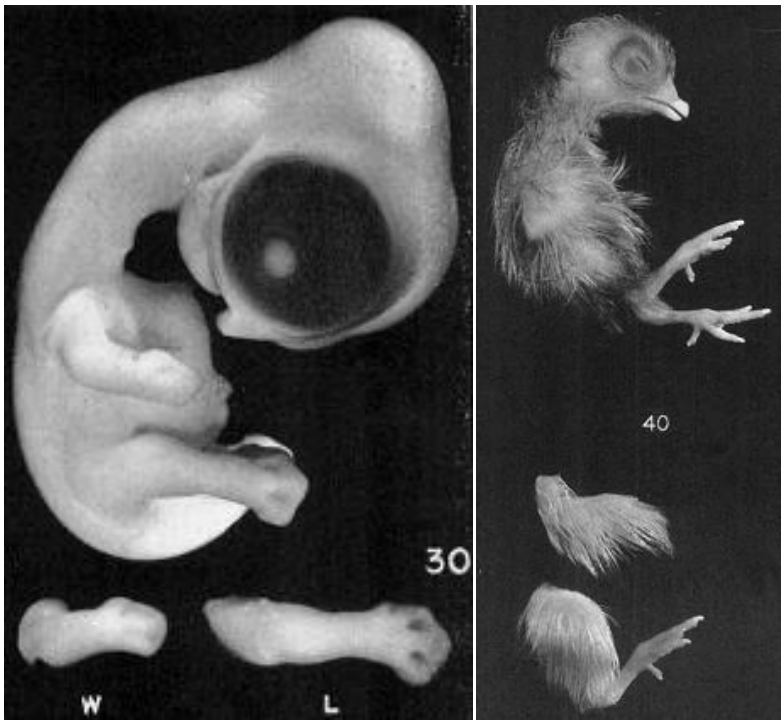

Figure 1.2: Stage 30 and 40 of the developing chick embryo as observed by Hamburger and Hamilton. Reprinted from Viktor Hamburger and Howard Hamilton: *A Series of Normal Stages in the Development of the Chick Embryo*. Copyright © 2005 John Wiley and Sons. Used by permission of the publisher, John Wiley and Sons (www.interscience.wiley.com).[19]

IV. RAMAN SPECTROSCOPY

Spectroscopy is a very wide topic, which uses electromagnetic radiation to study matter. In particular, Raman spectroscopy is a powerful analytical tool, which uses a monochromatic laser to excite vibrations and rotations in molecules. Therefore, Raman spectra provide a molecular fingerprint, in which various molecules will lead to different spectral profiles.[20]

The Raman effect is an inelastic scattering process that occurs due to the interaction between the analyte molecules and the photons. By definition, scattering is the collision of the photon with the molecule in which energy and momentum are transferred between the photon and the molecule. This scattering process may be elastic

(Rayleigh) or inelastic (Stokes and anti-Stokes) according to the change in energy experienced by the photons.[20]

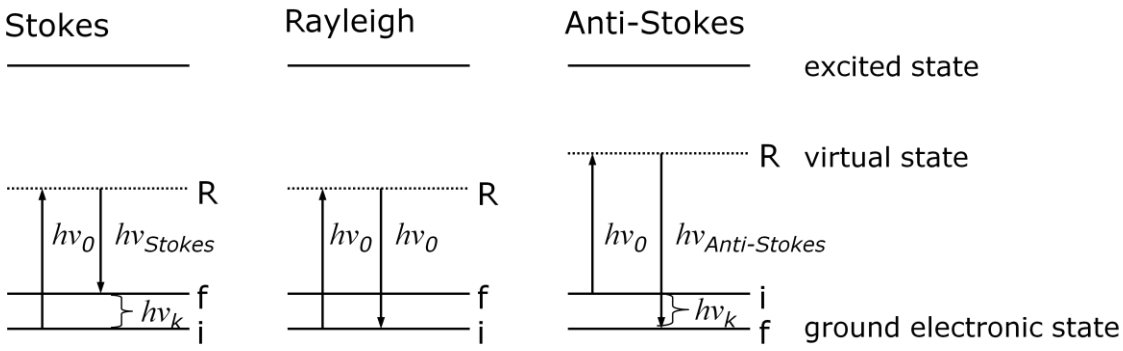

Figure 1.3: Shows a typical Raman energy diagram.[20]

As seen in Figure 1.3, during the interaction of the molecules with the excitation laser light, the potential energy of the molecules is raised to a virtual state (*R*) above the ground electronic state. Most of the molecules will immediately return to the ground state by emitting a photon of the same energy (ν_0) as the incident laser line. This is denoted as the Rayleigh scattering contribution. However, a very small fraction of the incident photons (1 in 10^{12}) will experience an inelastic scattering effect, the Raman Stokes (ν_{Stokes}) and anti-Stokes ($\nu_{Anti\text{-}Stokes}$) contributions. The Stokes portion of the Raman spectrum is produced when the molecules return to an excited vibrational/ rotational state. As a result, the scattered photon will have less energy than the incident one. Molecules that are already in an excited state will undergo similar effects in which the inelastically scattered photon will have more energy.[20]

The Raman effect arises due to the change in polarizability (α) of a molecule as a result of the interaction of molecules with the electric field vector (*E*) of the laser radiation (i.e., electromagnetic field), which induces a dipole moment change (μ):

$$\mu = \alpha E \tag{1.1}$$

Therefore, a change in the polarizibility of the molecule must be present during a vibration or a rotation in order for the mode to be Raman active. Thus, the symmetry of the molecule determines the activity of vibrational and rotational modes.[20]

During vibrations or rotations of a molecule, the polarizability is not constant and will change with the rotation or vibration frequency, ν_k, and time, *t*, according to equation (1.2).

$$\alpha = \alpha_0 + (\Delta\alpha)\cos(2\pi\nu_k t) \tag{1.2}$$

where α_0 is the equilibrium polarizability and $\Delta\alpha$ is its maximum variation. The incident electric field varies with time according to equation (1.3).[20]

$$E = E^o\cos(2\pi\nu_0 t) \tag{1.3}$$

Therefore, the induced dipole moment of the molecule is given by

$$\mu = [\alpha_0 + (\Delta\alpha)\cos(2\pi\nu_k t)]E^o\cos(2\pi\nu_0 t) \tag{1.4}$$

$$= \alpha_0 E^o\cos(2\pi\nu_k t) + \frac{1}{2}(\Delta\alpha)E^o[\cos(2\pi(\nu_0 + \nu_k)t) + \cos(2\pi(\nu_0 - \nu_k)t)]$$

The classical explanation for Rayleigh scattering (ν_0), anti-Stokes lines ($\nu_0 + \nu_k$), and Stokes lines ($\nu_0 - \nu_k$) is illustrated by equation (1.4).[20] This classical treatment implies that the intensities of the Stokes and anti-Stokes lines are equal; however, they depend on the relative number of molecules (*n*) in the original states.[20] Because of this dependence, the Boltzmann distribution is used to calculate the intensities (*I*) of the Stokes and anti-Stokes peaks, shown in Equation (1.5); where *h* is Planck's constant, *k* is the Boltzmann constant, and *T* is the temperature.[21]

$$\frac{I_{anti-Stokes}}{I_{Stokes}} = \frac{n_{excited}}{n_{ground}} = \frac{e^{\frac{-3h\upsilon}{2kT}}}{e^{\frac{-h\upsilon}{2kT}}} = e^{\frac{-h\upsilon}{2kT}} \tag{1.5}$$

Infrared (IR) radiation causes an induced dipole change in the molecule. Therefore, IR spectroscopy is considered a complementary analytical tool to Raman. If a molecule has a center of symmetry, the mutual exclusion rule is then applied. This states that if one normal mode is Raman active, then it will be forbidden in the IR and the opposite condition applies as well. The symmetry group may be used to determine if a normal mode vibration will be Raman or IR active.[20] The normal modes whose symmetry is the same as the function x, y, or z, will be IR active, while the Raman active modes will have x^2, y^2, or z^2 function.[20]

The selection rules for the Raman active vibrational modes are $\Delta\nu = \pm 1$ and $\Delta J = 0, \pm 2$ for linear molecules or $\Delta J = 0, \pm 2$, $\Delta K = 0$ and $\Delta J = 0, \pm 2$, $\Delta K \neq 0$ for symmetric top molecules, where K is the component of the angular momentum J. The rotational (R) Raman spectrum give anti-Stokes ($\Delta J = 2$) frequencies for linear molecules according to equation (1.6)

$$\Delta\nu_R = BJ'(J'+1) - BJ(J+1), \qquad (1.6)$$

where J' is the final quantum state and J" is the initial state. While substituting $J' = J" + 2$, the equation becomes

$$\Delta\nu_R = 2B(2J" + 3) \qquad (1.7)$$

These lines will appear at higher frequencies than the exciting laser frequency and therefore are denoted as the S branch. Hence, the intensities of these lines are directly determined by the populations of the initial state. The Stokes ($\Delta J = -2$) frequencies are given by Equation (1.8).

$$\Delta\nu_R = -2B(2J" - 1) \qquad (1.8)$$

These lines are denoted as the *O* branch lines because they appear at lower frequencies than the laser excitation line. The *Q* branch is then given by $\Delta J = 0$.[20]

The interpretation of Raman spectrum is based upon the law of conservation of energy as illustrated by Equation (1.9).

$$h(\nu_f - \nu_0) = E_f - E_i \tag{1.9}$$

This states that the frequency (ν_0) of the incident photon is scattered by a molecule in a quantum state *i* of energy E_i. Thus, the frequency of the outgoing photon (ν_f) will end in a quantum state *f* of energy E_f. In the Raman effect, the energy of the incident photon does not need to coincide with a quantized energy difference in the molecule. Therefore, any laser light frequency (e.g., visible, ultra violet) may be utilized.[21]

RAMAN DATA

Micro-Raman spectroscopy is a powerful, laser-based analytical technique that enables direct and non-destructive chemical characterization of molecules in a sample. Therefore, a Raman spectrum obtained from cells and tissues is an intrinsic molecular fingerprint of the sample, revealing detailed information about their chemical composition. Chemical composition of a location of interest may be investigated with micro-level spatial resolution by coupling the Raman spectrometer with a confocal microscope. Assessment of bone chemical composition is complicated because of tissue heterogeneity. In contrast with other well-established techniques for bone analysis such as X-Ray Diffraction (XRD) and Dual Energy X-Ray Absorptiometry (DEXA), micro-Raman spectroscopy may address the heterogeneity issue.

Raman peak position, intensity, full width at half maximum (FWHM), and integrated peak area are known to provide information on the cartilage/bone chemical

composition and structure. Micro-Raman maps may be used to determine, analyze, and quantify the following cartilage/bone properties:

a) age of mineral crystals and carbonate content in cartilage/bone

As mentioned above, cartilage/bone tissue is a composite of an organic matrix and an inorganic mineralized component. The mineral fraction of cartilage/bone is carbonated calcium phosphate [$Ca_5(PO_4, CO_3(OH)$], commonly described as hydroxyapatite (HAP). Ions such as fluoride, chloride, and magnesium may also be incorporated into the crystal lattice of the mineralized matrix, depending on the chemical environment and tissue history. For example, carbonated ions (CO_3^{2-}) substitute for two anionic sites in the HAP structure: monovalent OH^- sites and trivalent phosphate PO_4^{3-}. They are known as type-B ($\nu_1(CO_3^{2-})$ mode at 1070 cm^{-1}) and type-A ($\nu_1(CO_3^{2-})$ mode at 1103 cm^{-1}) substitutions. In contrast to cartilage, mature bone generally contains more carbonate, and the type-B carbonate represents the major species.[22,23] The ratio of the amount of type-B carbonate and the amount of phosphate will allow estimating the age of mineral crystals and the carbonate content in the samples (by calculating the intensities ratio and the integrated areas ratio: I(CO_3^{2-} band at 1070 cm^{-1}) / I(PO_4^{3-}band at 960 cm^{-1}).[23,24]

b) inorganic to organic cartilage/bone components ratio (i.e., degree of mineralization of the collagen matrix) and **possible losses in any of the two cartilage/bone components**.

The inorganic component (i.e., the mineral) is usually represented by the strong PO_4^{3-} vibrational modes in the 920-980 cm^{-1} spectral range, while the organic component of the bone (i.e., the collagen matrix) corresponds to the amide I vibrational modes in the 1600-1700 cm^{-1} region.[24] In contrast, cartilage tissue contains both type I and type II (1200-

1300 cm^{-1} and 1600-1700 cm^{-1}) collagen fibers. The integrated area of the peaks corresponding to the inorganic components may be compared with the ones corresponding to the organic components and the ones determined for the control samples to estimate the mineral to matrix ratio.

Possible changes in the spectral profile of the vibrational modes of

- the PO_4^{3-} group: ν_1(960 cm^{-1}), ν_2(430-450 cm^{-1}), ν_3(1030-1040 cm^{-1}), ν_4(580-590 cm^{-1})[24,25]
- the CO_3^{2-} group : ν_1(1070 cm^{-1})[24,25,26]
- the collagen amide I: 1600-1700 cm^{-1} [24,25], 1400-1470 cm^{-1} [24,25,26]
- the collagen CH groups: stretching modes at 2800-3100 cm^{-1} [24,25]
- the collagen amide III: 1200-1300 cm^{-1} [24,25]

may also be examined to determine if there are any losses in the inorganic and organic components of cartilage/bone when compared to the control. The Raman spectrum of the embedding material may be recorded separately and used as a reference to ensure the correct assignment of the observed bands.[26,27]

c) mineral crystallinity

The bandwidth of the $\nu_1(PO_4^{3-})$ symmetric stretching mode at about 960 cm^{-1} may be correlated with crystal size. The FWHM of this peak was observed to steadily increase with decreasing crystal size and smaller crystallinity, i.e. less ordered crystal.[28,29] Akkus *et al*. showed that the mineral crystallinity of normal rat cortical bone could be approximated as $\approx$ 1/bandwidth of the 960 cm^{-1} peak.[29]

V. X-RAY FLUORESCENCE MICROSCOPY

X-ray fluorescence spectroscopy is a non-destructive, analytical technique that allows for mapping of the elemental composition of a sample.[30] High-energy X-rays bombard the sample causing the removal of an electron (photoelectric effect) located in the inner orbitals of the atom. The atom becomes unstable upon the loss of this inner electron. As a result, an electron from a higher energy level fills the empty orbital. Due to the energy difference between the two orbitals, a photon is released causing an X-ray fluorescence emission characteristic to the specific atom. Morphological features of the sample may be simultaneously identified by attaching an optical microscope to the X-ray fluorescence system.[30]

VI. FLAME ATOMIC ABSORPTION SPECTROSCOPY

The flame atomic absorption spectroscopy technique (Figure 1.4) is credited to Sir Alan Walsh in 1955.[31] This technique makes use of atomic absorption in order to determine the concentration of a specific metal in a sample. A chemically digested liquid sample introduced into the nebulizer to be first aerosolized and then atomized (i.e., free, unexcited ground state atoms) during the combustion processes sustained by the acetylene-air gas mixture. The electrons absorb the energy emitted from a hollow cathode lamp (i.e., light of a given wavelength), in which the radiation is specific to the electronic transition of the metal; therefore, allowing for metal selectivity. The Beer-Lambert Law is applied in order to determine the metal concentration due to the reduction in light intensity. A photonmultiplier detects the amount of light transmitted through the sample.

As in most analytical instrumentation, the flame atomic absorption spectrometer must be calibrated and set to specific conditions for the element of interest. A calibration curve is prepared by analyzing known concentrations of the metal analyte and plotting their absorption values against the known concentration. The unknown samples concentrations are then extrapolated from the resultant calibration curve.

Figure 1.4: Flame atomic absorption spectrometer owned by the Department of Chemistry at Wright State University. (photo courtesy of Garrett VanNess)

2. EXPERIMENTAL

I. WHITE LEGHORN STRAIN CHICK EMBRYO MODEL

Six-day old fertile-specific and pathogen free (SPAFAS) white leghorn strain chick embryos were purchased from Charles River Laboratories International, Inc. Upon arrival, the air sac poles of the eggs were disinfected by wiping the egg surfaces with 70% isopropanol. The location of the air sac was determined by candling using an external light source. Holes (1 mm^2) were drilled in the external shell only to leave the internal membranes intact. Tape sealed the holes to prevent air and contaminants from entering.

The chick embryos were incubated for 20 days at 38 ± 1°C with the relative humidity levels at 50-55%. A drip pan filled with sterile water controlled the humidity level. The incubator was equipped with an automatic turner , which changed the embryo position every 4 hours to ensure an even exposure to temperature and humidity. The developmental phase and vasculature development of the embryos were evaluated by candling, every 48 hours. Chick embryos without observed developing capillaries were removed from the incubator and were not used for any further evaluation.

IN OVA INJECTIONS

Injection solutions were prepared as solutions with single metal concentrations (Pt $^{(IV)}$ in the form of $H_2[PtCl_6]•6H_2O$, Rh $^{(III)}$ in the form of $RhCl_3$, and Pd $^{(II)}$ in the form of $PdCl_2$ salt solutions (SPEX-CertiPrep) or as PGM mixture (an equal portion of all three

PGMs). Solutions for the single metal injections ($Pt^{(IV)}$, $Rh^{(III)}$, $Pd^{(II)}$) were prepared at the following concentrations: 0.1, 1.0, 5.0, or 10.0 ppm and were diluted with phosphate buffer saline (PBS) solution. The PGM mixture injection solutions (0.1 ppm and 1.0 ppm) were prepared by combining each metal at a concentration of 0.1 and 1.0 ppm and diluting with PBS solution. All solutions were adjusted to a pH of 7.2 with 0.1 N HCl and 0.1 N NaOH. The PGM treatment solutions were filtered through a 0.2 μm filter (Whatman GD/X) to remove particulate matter and bacteria.

The injection solutions were administered on the 7^{th} and 14^{th} day of gestation period according to the developmental stages determined by the HH guide.[19] The doses (1 mL) were injected with a hypodermic needle through the previously prepared 1 mm^2 hole into the air sac. The experimental design included ten replicates for each treatment including two control sets (i.e., no injection and PBS solution treatment at the same pH value).

SAMPLE COLLECTION

The National Institute of Health Guidelines for the Care and Use of Laboratory Animals were followed to harvest the chick embryos. The embryos were sacrificed on the 20^{th} day of incubation by decapitation upon egg removal from incubator. Tibiotarsus samples were immediately collected and segregated for different analysis: histology, flame atomic absorption spectroscopy, X-Ray fluorescence spectroscopy, and micro-Raman spectroscopy.

PATHOLOGICAL ANALYSIS

The gross pathology and microscopic pathology observations regarding abnormalities and deformities of harvested chick embryos were documented. Gross

pathology of each chick embryo before dissection was recorded using an Olympus digital camera. Microscopic pathology was conducted on 4 μm thick cross-sections of the bone using a light microscope and images were recorded using a Magnafire SP Digital Camera. The bone slide preparation for histological studies is described below.

MICROSCOPE SLIDE PREPARATION

Micro-Raman spectroscopy slide preparation: The soft tissues were cleaned from the tibiotarsi, rinsed in PBS, and immediately placed in 10% phosphate buffered formalin. The phosphate buffered formalin fixed the tissue and hindered post mortem conditions, such as petrification and autolysis of cells. The tissue dehydration used a graded series of alcohols: 50% ethanol for 60 minutes, 70% ethanol for 60 minutes, 95% ethanol for 30-60 minutes, absolute ethanol for 30-60 minutes, and absolute ethanol for 30-60 minutes. Prior to embedding the tissue, a clearing agent removed any remaining alcohol (two times for 30-60 minutes each) since the alcohol used for the dehydration and the paraffin used for the embedding do not mixture. A Tissue Tek infiltrator and dispenser was used to embed the tissue in paraffin wax. Next, the embedded tissue was placed in an oven at 60°C for 60 minutes to permit the wax to fill the empty spaces within tissue. The infiltrated tissue specimen was positioned in the center and towards the bottom of the mold to maintain the same position of proximal and distal epiphysis in a labeled Peel-Away mold filled with melted paraffin. After the paraffin mold cooled, a Spencer microtome was used to cut the fixed and embedded bone into 4 μm slices. The paraffin tissue, sectioned in ribbons, was carefully emerged in a water bath at 40-44°C. A thin layer of albumen was spread over a microscope slide and the shiny side of the paraffin embedded tissue was placed on the microscope slide. The slides supporting the

specimens were heated overnight at approximately 50°C on a tissue warmer to facilitate the coagulation of albumen. The prepared slides were stored in a clean, dry place for the micro-Raman measurements.[32]

Histological slide preparation

The previously-described micro-Raman spectroscopy slide preparation was followed with an additional hemotoxylin staining procedure. After the tissues were embedded, the paraffin wax was removed by using a hydration series of ethanol (95%, 70%, and 50%) washes followed by a distilled water rinse. The hemotoxylin stain was used in the last step of the hydration series. The water was removed by using a dehydration series process employing ethanol (95%), eosin stain, ethanol (70%), ethanol (50%), and tap water until a blue color persisted. Each of the above ethanol rinses were approximately 3 minutes. The removal of water is necessary in order for the cover slip to adhere to the tissue. The stained slides were then moistened with a clearing agent and mounting medium was placed directly on the tissue. Slowly with gentle pressure, the cover slip was lowered to the slide to avoid air bubbles. The prepared slides were placed on a slide warmer in an upright position to dry. The dried slides were stored for histological analysis.[32]

CHANGES IN CHONDROCYTE LENGTH

The bone slices were analyzed for chondrocytes length using Magnafire SP Digital Camera software. The largest diameter across the chondrocyte was measured and recorded in triplicate for 50 randomly chosen cells in each slide.

STATISTICAL ANALYSIS

One-Way Analysis of Variance (ANOVA) SPSS (Statistical Package for the Social Sciences) statistical package was used to test for relationships between concentration of metals in PGM treatments and tibiotarsus chondrocyte size. Significance level was determined at $p \leq 0.05$ probability by Student-Newman-Keuls multiple comparison test.

II. RAMAN INSTRUMENTATION[33]

A LabRAM HR800 (Horiba Jobin Yvon, Inc.) instrument coupled with a high resolution confocal optical microscope (Olympus, high stability BX41) was used for the acquisition of Raman spectra on the bone samples.

Figure 2.1 shows the Raman instrument with the cover removed. An internal He-Ne laser (Horiba Jobin Yvon, Inc.) and the corresponding optical entrance are located on the backside of the instrument. The He-Ne laser is polarized vertically (500:1) and has a power output of 22.5 mW for the 632.817 nm wavelength. The design of the instrument also allows for the use of external lasers, which would enter the optical cavity through a second laser entrance. The laser beam is directed into the iris by two mirrors denoted here by M_1 and M_2, which may also be used for the laser alignment. After passing through the iris, the beam enters an interferential pass-band filter that removes the plasma lines of the laser and leaves only the 633 nm light. The laser beam meets a set of density filters, which help reduce the laser intensity if necessary. The density filters are housed in a wheel which contains six neutral filters with the following optical densities: 0.3, 0.6, 1, 2, 3, and 4. The beam then encounters a second iris and is focused by the lens L1 onto a pinhole H1 (spatial filter for point mode) with the help of the M6 mirror.

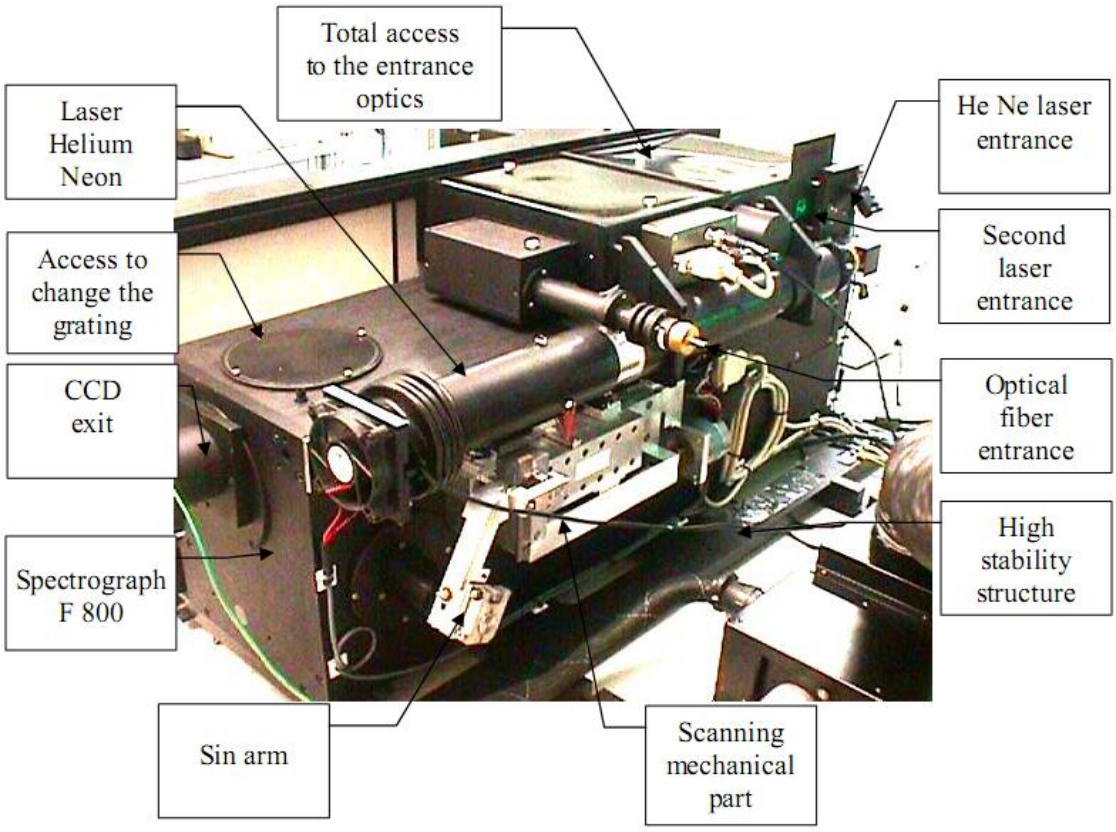

Figure 2.1: The main components of the LabRam HR800 instrument with the cover removed. Reprinted from Horiba Jobin Yvon: *HR800 User Manual*. Used by permission of the publisher, Horiba Jobin Yvon.[33]

The laser injection rejection system (LIRS) directs the laser beam onto the notch filter with aid from the mirror M_8. A spacer allows for the notch angle to be changed, so that the beam is completely reflected towards the sample. Lens L_3 converges the beam onto mirror M_9, which is then directed to the sample via the optical microscope objective. The back scattered radiation follows the same pathway up to the notch filter. The Rayleigh scattering is reflected at the notch filter (i.e., the excitation laser line is rejected), while the inelastically scattered light passes through. The image of the Raman beam is then formed by lens L_3 onto the confocal hole, which functions as an adjustable

pinhole. The confocal hole allows for the separation of the signal from each layer of a layered sample as well as for removing any contributions from the surrounding medium.

The resulting magnification between the sample and the objective can be calculated by multiplying the objective magnification used for measurements by 1.4 (e.g., 100 x 1.4 for the 100x objective). The 1.4 magnification factor is represented by the focal length (250 mm) of lens L_3 divided by the tube length (180 mm) of the Olympus objectives.

The image from the confocal hole is then projected by lenses L_7 and L_8 onto the slit S_1 of the spectrograph, which reduces the image by a factor of 5. The shutter, which is located behind the slit S_1, controls the signal that enters the spectrograph. Once the image enters the S_1 slit, the beam is reflected by mirrors M_{12} and Ms_1. A spherical mirror SP_1 of a focal length of 800 mm makes the beam parallel and reflects it onto the grating. The resultant first order diffraction is collected by mirror SP_2 of an 800 mm focal length, which then focuses the beam onto an open electrode thermo-electric cooled (CCD detector operating at -69°C). Figure 2.2 illustrates the beam pathway through the instrument.

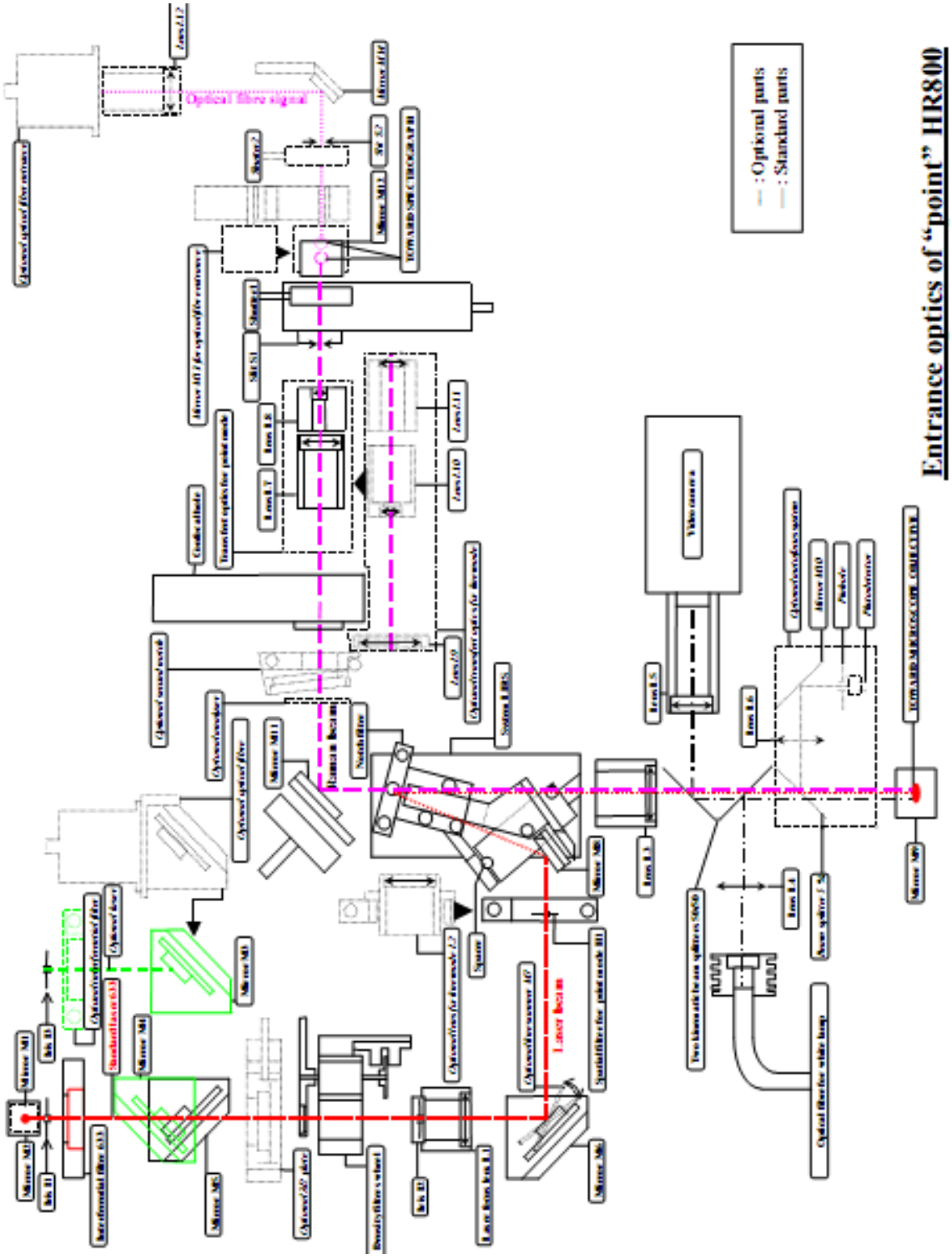

Figure 2.2: Schematic showing the pathway of the laser through the LabRam HR800. Reprinted from Horiba Jobin Yvon: *HR800 User Manual*. Used by permission of the publisher, Horiba Jobin Yvon.[33]

There are two kinematic gratings located on the spectrograph, namely 1800 or 600 grooves/mm, and mounted onto kinematic interchangeable holders. When the 1800 grooves/mm grating is in use, an internal laser diode can be redirected along the optical path towards the entrance optics. This is employed for the alignment of the confocal hole and the position of the laser beam on the sample. A sine bar mechanism is used to cover a scanning range determined by the grating. For the 1800 grooves/mm grating, the scanning range is 0 – 950 nm, while for the 600 grooves/mm, the scanning range is 0 – 2850 nm due to the smaller amount of grooves. A grating spectrograph will have a relatively constant dispersion if measured in nm, but when measuring in cm^{-1}, there is a strong non-linear $1/\lambda^2$ dependence as illustrated in Equation (2.1).

$$\Delta\upsilon\left(\mathrm{cm}^{-1}\right) = \frac{10^7}{\lambda^2(\mathrm{nm})}\Delta\lambda(\mathrm{nm}) \tag{2.1}$$

Resolution depends on the dispersion, the slit width, and the image dimension on the CCD. The image dimension on the CCD is calculated using Equation (2.2),

$$W_i = W_s \frac{\cos i1}{\cos i2} \tag{2.2}$$

in which W_i is the dimension of the image slit on the CCD, W_s is the slit width, i1 is the incident angle on the grating, and i2 is the diffracted angle on the grating. The accuracy using the 1800 grooves/mm grating is 1 cm^{-1} in the 450 – 850 nm spectral range. The repeatability under normal operating conditions (temperature: 20-25 with variations of ±1°C and humidity: ≤ 75%) is one pixel with the CCD camera.

The LabRam HR800 is equipped with a color video camera (UEye, UI-1540-C) and a fiber optic white light source (Euromex, EK-1), which are used in conjunction with the optical microscope. The white light source utilizes a halogen bulb and has a

continuous brightness control that allows for intensity adjustment to view the sample in real time. A 50/50 beam splitter must be placed between lens L_3 and mirror M_9 to allow for the white light to reach the sample and to send the image of the sample to the video camera with the help of lens L_5.

The LabRam HR800 instrument is equipped with a motorized XY mapping stage (travel range: 100 x 80 mm^2 and step size: 0.1 µm) that allows for the use of Raman mapping and extended video options. The optical Raman microscope is equipped with a Z motor that can be controlled by either the instrument software or joystick similarly to the XY stage. This Z-motion (resolution: 0.1µm) option facilitates the depth profile point Raman measurements on a sample and the signal-to-noise ratio optimization of point measurements during Raman mapping (through the AutoFocus option: ± 30 µm).

The Raman mapping feature collects Raman spectra at predetermined points along the sample and then compares the relative intensities of the Raman peaks of interest to create a color coded image. The color coded image can then be used to interrogate the molecular composition and heterogeneity of a sample. The Raman maps can be collected in various shapes (square, rectangle, line, random points) and sizes with pre-set increments. The AutoFocus option can be employed to account for height differences within the sample at each point in the Raman map. The SWIFT option allows for rapid data collection (as fast as 7 ms per point) by moving the stage continuously during measurements, while the regular Raman mapping option stops and collects a spectrum at each predetermined point. The extended video option can be used to expand the viewing area of the objective by moving the XY stage as permitted by the XY domains. The viewing areas are then spliced together to form the final extended video image.

VII. RAMAN MEASUREMENTS

The Raman system was calibrated before each measurement using the 521 cm^{-1} optical phonon mode (2 transverse and 1 longitudinal) of the lattice structure of silicon.[34] The silicon sample was placed onto a glass microscope slide and positioned on the sample stage. A long working distance 100x objective (Olympus, LMPlanFLN) was used to focus the laser beam on the sample and to collect the backscattered Raman signal. The 633 nm output (22.5 mW) of a He-Ne laser was used as the excitation line. The confocal hole was set at 300 μm, and the backscattered Raman signal was recorded using a 600 grooves/mm holographic grating, a number seven spacer, and an open electrode thermo-electric cooled CCD detector. The Raman signal at 521 cm^{-1} was optimized (approximately 52,000 arbitrary units) using the real time spectrum adjustment mode. The spectrometer was centered at 730 cm^{-1} during the real time measurements to avoid the laser excitation line.

The microscope slides supporting the bone samples were placed onto the microscope stage and imaged using the 100x objective. Paraffin wax slides were also measured as a control. All Raman spectra were collected in the 100 – 2000 cm^{-1} fingerprint spectral area using the 633 nm He-Ne laser. The laser power at the sample was 15 mW. All other instrument settings were the same as for the silicon standardization procedure. Point measurements were first obtained on each sample to determine suitable acquisition times (3 s). The signal was averaged over two cycles to reduce the noise of the spectra for each point measurement.

Once the point measurements were completed, a 15 μm cross-section was selected for Raman mapping measurements on each bone sample. The Raman map was collected in incremental segments to allow the instrument to rest and to prevent loss of data (Figure. 2.3). The auto focus feature was employed to account for the difference in height at various points on the bone sample and to optimize the signal-to-noise ratio. This experimental setup allowed for the analysis of a bone sample to be completed in five to ten days, depending on the width of the bone section. The Raman maps were collected using the LabSpec (v. 5) software and processed with the help of the Origin 8 software package. All spectra were baseline corrected by the user defined option with 20 anchor points and interpolated using the spline method.

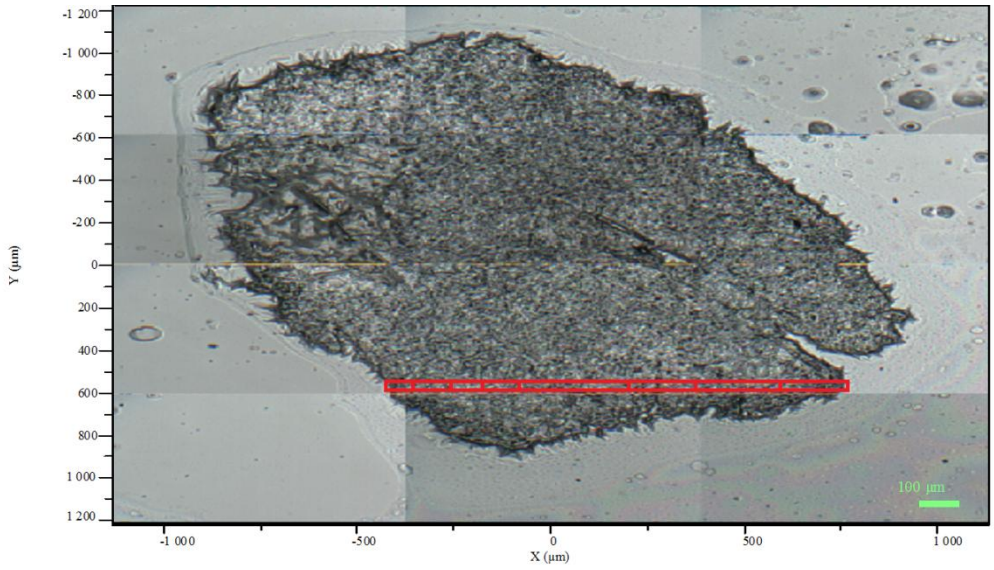

Figure 2.3: Optical image of a control bone sample recorded using the extended video mode option. The red areas represent the Raman mapping segments of 15 μm wide cross-section.

IV. X-RAY FLUORESCENCE

The chick embryo tibiotarsi were cut longitudinally and placed in the X-Ray fluorescence sample holders that contained an X-Ray specific film. The samples were

strategically mounted to study both the internal and external sections of the bone as shown in Figure 2.4. A Horiba XGT-7000 X-Ray Analytical Microscope was used to collect the X-Ray images and spectra.

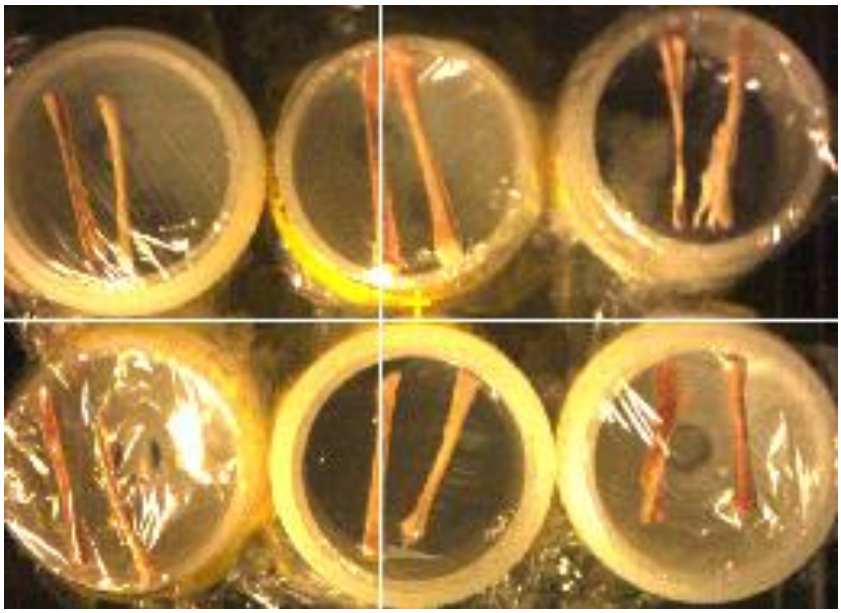

Figure 2.4: Picture showing the placement of the tibiotarsi samples in order to study both the internal and external sections.

V. FLAME ATOMIC ABSORPTION SPECTROSCOPY

Bone samples which were not fixed and embedded were used to determine the total calcium content via flame atomic absorption spectroscopy (FAAS, Varian AA240FS). One bone sample for each single metal dose at 1 ppm and one bone sample for the PGM mixture at 1 ppm were prepared for FAAS analysis. Prior to sample preparation, two bone samples for each treatment were preserved in the freezer. The wet weight was recorded and the dry weight was determined by drying in an oven at 80°C for 72 hours.

All glassware was cleaned by an acid bath, base bath, and finally autoclaving. All utensils and work sufaces were sanitized using ethanol to minimize cross-contamination. The dried bone samples were ground in a beaker with a glass rod in order to allow the

chemical digestion to proceed quickly. The sample digestion was started with the addition of nitric acid (Fisher Scientific, OPTIMA grade) and covered with a watch glass for approximately 15 minutes. The predigested sample and beaker were placed on a hot plate and heated to reflux gently for approximatley one hour at 125°C. After the sample was removed from the hot plate and allowed to cool to 80°C, 3 mL of hydrogen peroxide (H_2O_2, 30%) was added to the solution. The beaker was returned to the hot plate at a temperature of approximately 80°C until the digestion was complete when the solution became clear. The watchglass was removed and the heating was continued until almost all the liquid has been evaporated. The sample was immediately removed to prevent burning. Once the sample was near dryness, 8 mL of nitric acid was added while swirling. The digested sample was quantitatively transferred to a 10-mL volumetric flask and diluted to volume with nitric acid (OPTIMA, grade).

The acidified, digested samples were then analyzed for calcium concentration using a Varian Fast Sequential Flame Atomic Absorption Spectrometer (AA240FS), equipped with an air-acetylene burner and a calcium hollow cathode lamp (5 mA). The operating conditions were set as recommended by the manufacturer: wavelength (422.7 nm), slit width (0.7 nm), air flow rate (2.00 L min^{-1}), and acetylene flow rate (13.50 L min^{-1}). Both the sample measurement acquisition time and delay time between each measurement were 3 seconds. Each sample was measured in triplicate and the absorbance values were averaged before extrapolating the calcium concentration from the calibration curve. A blank solution containing 2% nitric acid was introduced between each sample.

A FAAS reference calcium standard solution of 1.0 x 10^3 ppm (Fisher Scientific) was used for the preparation of seven calcium standards of 0.05, 0.10, 0.50, 1.00, 2.5,

5.00, and 10.00 ppm. Each sample contained 2% nitric acid (Optima grade, Fisher Scientific) and 0.05% lanthanum chloride (Fisher Scientific). Samples were diluted 100x (PGMs 1.0 ppm) or 200x (Pt 1.0 ppm, Rh 1.0 ppm, Pd 1.0 ppm). A sample spiked with 0.5 ppm calcium (92% recovery) was analyzed to check for matrix interferences and a duplicate sample was analyzed (100.1% recovery) to verify accuracy and precision.

3. RESULTS

Exposure to PGMs affected the morphology, calcium distribution, and calcium concentrations of the tibiotarsi of chick embryos. As the dose of the PGMs was increased, the affects to the tibiotarsi were also more pronounced. The correlation between metal exposure and bone morphological changes in developing chick was verified with Micro-Raman spectroscopy analysis. In addition, the changes to calcium distribution along the internal and external longitudinal sections of the bone were shown by the histopathological analysis and X-Ray fluorescence images. The average calcium amount per gram of tibiotarsus weight for each sample was determined by FAAS measurements.

I. HISTOPATHOLOGICAL ANALYSIS

Gross observations

Gross pathological observations provided evidence on the significant impact of embryonal exposure to PGMs. The brain was protruding from the underdeveloped skull with the 5.0 ppm Pt treatment (Figure 3.1A). Chick embryos that were exposed to 10.0 ppm Rh exhibited distinct abnormalities such as development of fully functional pectoral and abdominal organs exterior to the body cavity. The lethal dose (LD_{100}) for all PGM treatments was found to be 10.0 ppm, while LD_{50} was reached for PGMs concentrations of 5.00 ppm. The chick embryos exposed to 10.0 ppm doses of PGMs exhibited a black coloration characteristic to tissue necrosis (death).

Figure 3.1 (label A and B): Abnormally developed chick embryos. A) Brain tissue exposed due to the underdeveloped skull for the 5.0 ppm Pt treatment. B) Internal organs found outside the abdominal and pectoral cavities as a result of bone malformations in embryos treated with 10.0 ppm of Rh.

Histological analysis

Histological analysis of the bone cross-sections was used to determine the size of the bone cells in tibiotarsi. The average chondrocyte lengths decreased in all PGM treatments in comparison with the control specimens (Figure 3.2). The smallest chondrocytes were detected for the 1.0 ppm Rh treatment.

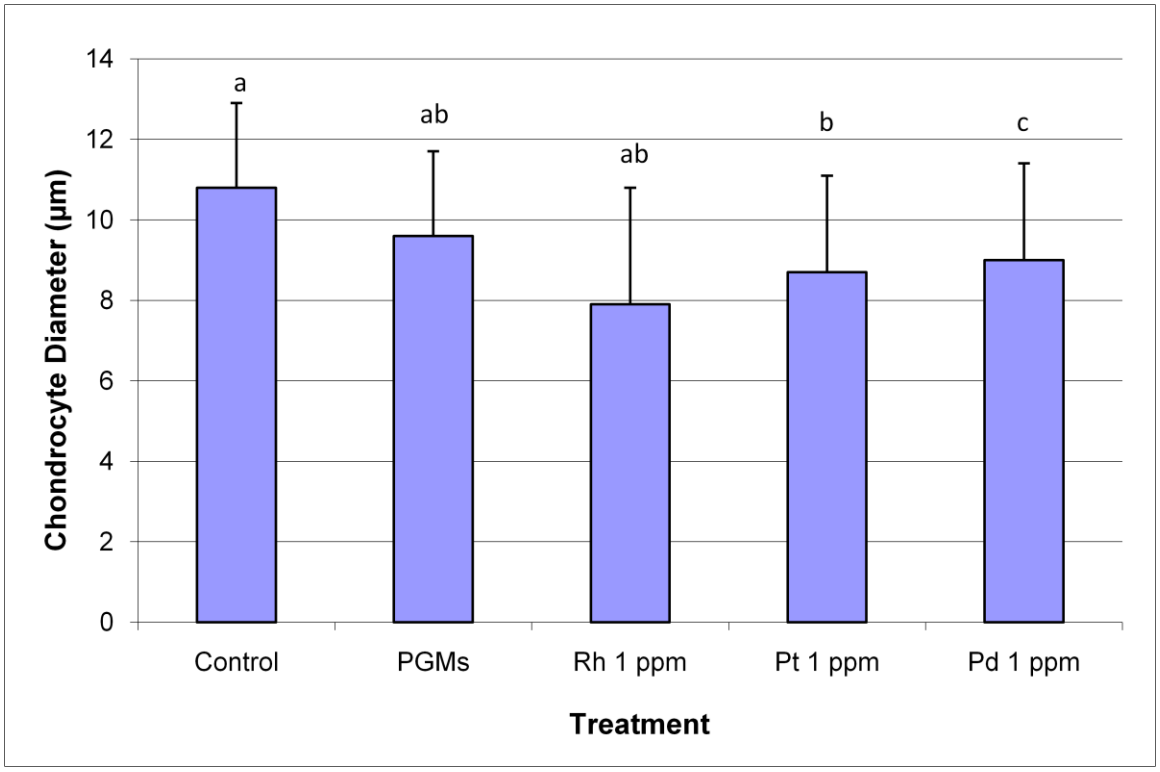

Figure 3.2: Length of chondrocyte diameters in the tibiotarsus of chicks embryos exposed to PGMs. The bar graphs represent the chondrocytes diameter ± SD based on average diameter of 50 chondrocytes per 3 slides from each of the metals. Diameters with the same letters^{abcd} were not statistically different at $p \leq 0.05$ probability level as determined by Student-Newman-Keuls multiple comparison test.

II. RAMAN DATA

Raman spectra and optical images were obtained from all bone cross-sections of 1.0 ppm PGM treatments along with three controls (i.e., no injection.PBS treatment, and paraffin wax). The third control slide supporting a paraffin wax section was measured to determine the possible contributions of the embedding material to the Raman spectra of the bone samples of interest. Figure 3.3 and Figure 3.4 show the optical image (100x objective) and the Raman spectrum, respectively, obtained from the paraffin wax control of the same thickness as the bone cross-section samples. The peaks occuring at 1420, 1442, and 1464 cm^{-1} were used to produce the original Raman maps (maps A in the following figures). This allows for a quick determination of the location of the higher

phosphate content areas. Figures 3.5 and 3.6 show the typical micro-Raman spectra of the no injection control and the 1.0 ppm PGM mixture treatments when located in an area of high phosphate content as noted by the $\nu_1(PO_4^{3-})$ vibrational mode. The assignments of all relevant vibrational bands are found in Table 1.

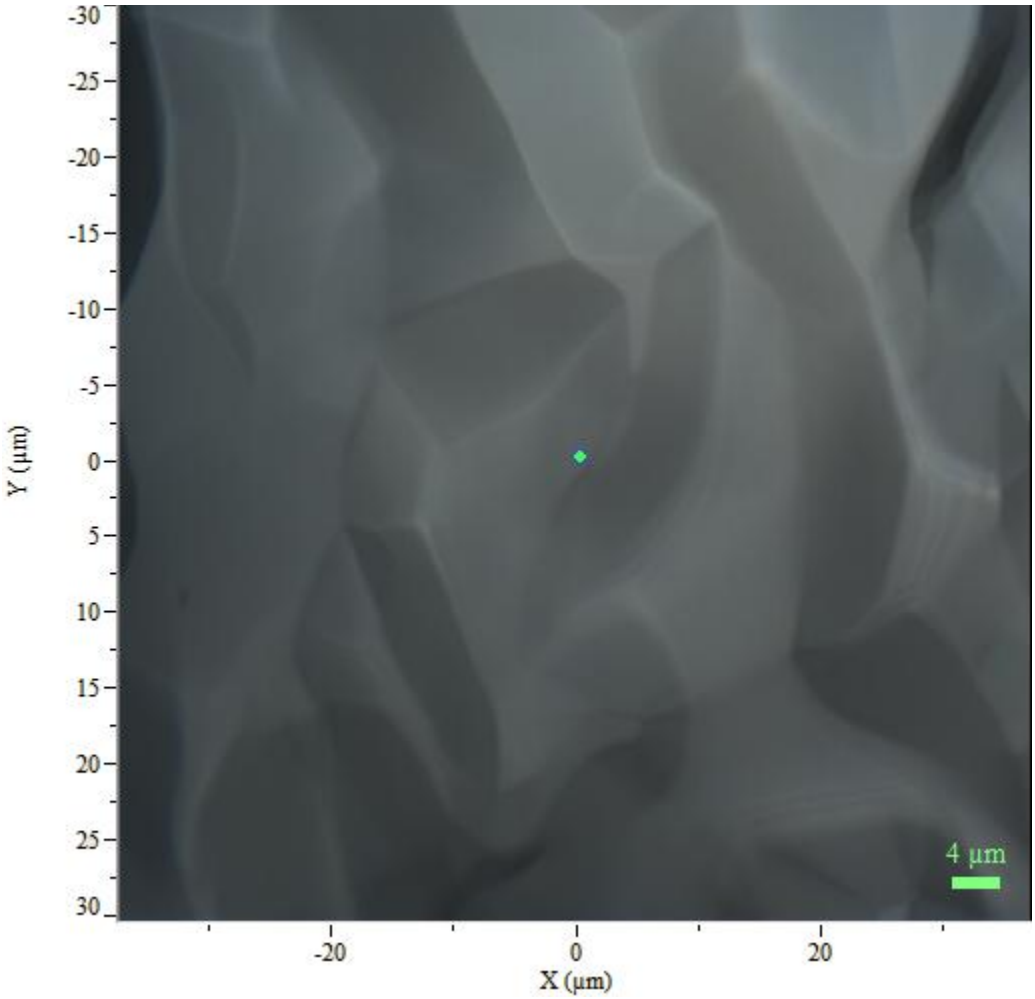

Figure 3.3: Optical image of the paraffin control sample recorded using the 100x objective of the confocal Raman microscope.

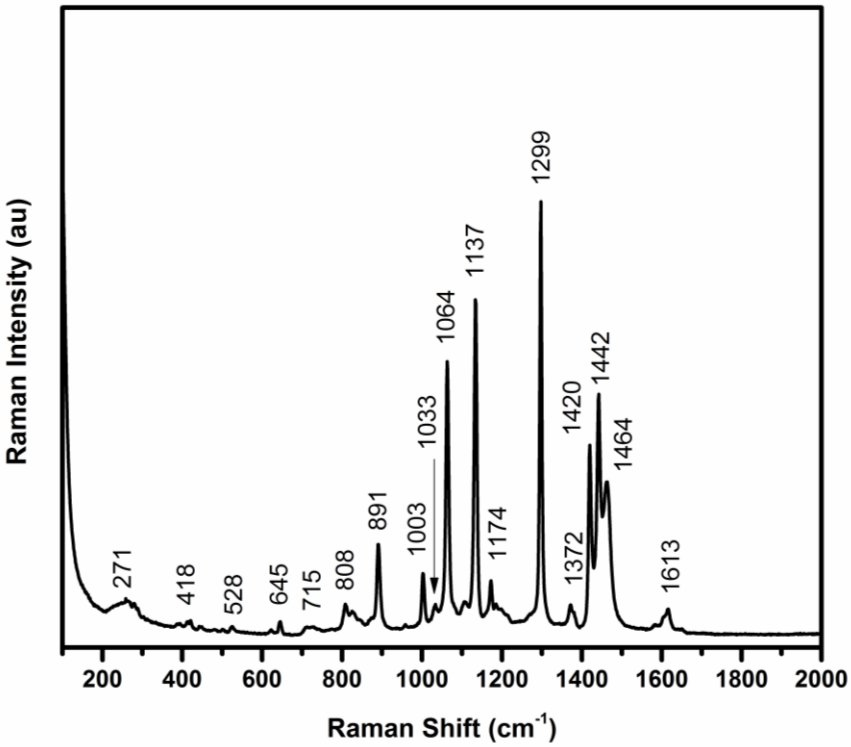

Figure 3.4: Micro-Raman spectrum of the paraffin wax control along with all peaks of interest assigned.

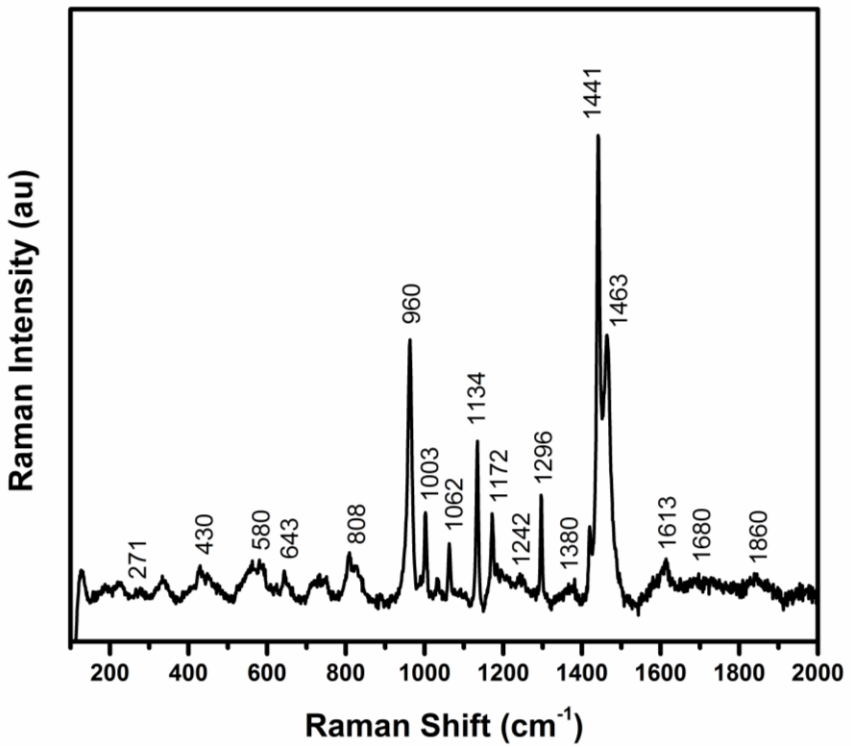

Figure 3.5: Micro-Raman spectrum from the no injection control sample with all the peaks of interest assigned (PO_3^{4-} at 960 cm^{-1}, CO_3^{2-} at 1070 cm^{-1}, amide I at 1680 cm^{-1}

and the paraffin modes). It should be noted that the CO_3^{2-} at 1070 cm^{-1} overlaps with the paraffin vibrational mode at 1062 cm^{-1}.

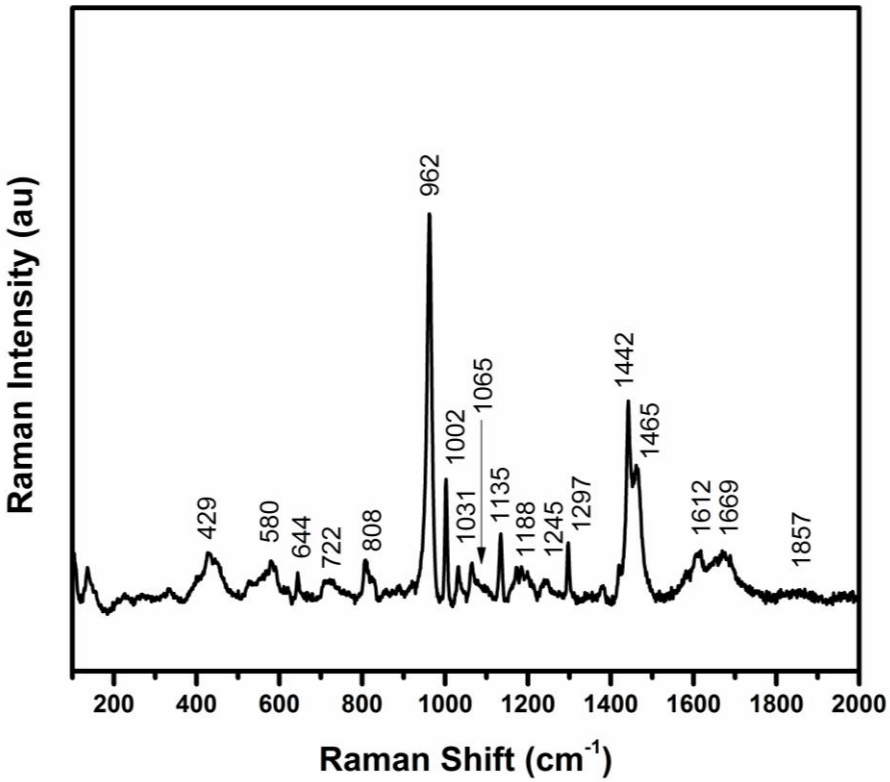

Figure 3.6: Micro-Raman spectrum from the 1.0 ppm PGM mixture sample with all the peaks of interest assigned.

Table 3.1: Tentative Raman band assignments for the tibiotarsi samples.
(Abbreviations: vs, very strong; s, strong; m, medium; w, weak; vw, very weak; sh, shoulder; ν, stretching; δ, bending; γ, twisting).
*Non-referenced assignments were observed in the paraffin control to determine its contribution in the treated samples.

Band Position (cm^{-1})	Tentative Band Assignment
271	paraffin
418	paraffin
430[35]	ν_2 (PO_4^{3-}) – symmetric P-O stretch
528	paraffin
583[25]	ν_4 (PO_4^{3-}) – symmetric P-O stretch
590[25]	ν_4 (PO_4^{3-}) – symmetric P-O stretch
609[25]	ν_4 (PO_4^{3-}) – symmetric P-O stretch
645	paraffin
673[25]	δ (CCH); ν (CCO)
715	paraffin
808	paraffin
815[25]	ν (C-O-O); ν (C-C) of backbone skeletal vibrations

855[25]	ν (C-C) of hydroxyproline ring
876[25]	ν (C-C) of proline ring
891	paraffin
921[25]	ν (C-C) of proline ring
961[25]	ν_1 (PO_4^{3-}) – symmetric P-O stretch
1004[25]	Phenylalanine, paraffin
1032[25]	Phenylalanine, paraffin
1045[25]	ν_3 (PO_4^{3-}) – antisymmetric P-O stretch
1063[26]	ν (CC) skeletal stretch, paraffin
1071[25]	ν (CO_3^{2-}) – type B
1103[19,20]	ν_1(CO_3^{2-})
1133[26]	ν (CC) stretch, paraffin
1172[26]	ν (CC) stretch, paraffin
1175[25]	ν (CCC) – out of phase, paraffin
1205[25]	Tyrosine
1245[25]	ν (amide III)
1270[25]	δ (NH) – amide III
1296[26]	CH_2 deformation, paraffin
1318[25]	γ (CH_2)
1340[25]	δ (CH_2)
1380[25]	δ (CH_2), paraffin
1418[26]	CH_3 deformation
1418[25]	ν (COO^-)
1426[25]	δ (CH_2), paraffin
1441[26]	CH_2 deformation
1451[25]	δ (NH_2)
1463	paraffin
1613	paraffin
1658 [20,25]	ν (C=O) amid I (α-helix)
1667 [20,25]	Amid I (β sheet)

The optical image (10x objective) of the no injection control bone sample is shown in Figure 3.7. The bone tissue section marked in red delimits the area studied using the Raman mapping feature. The Raman mapped areas were determined by finding an area of phosphate within the cross-section. The Raman maps used for this study are depicted in Figure 3.8. The maps are generated by comparing a) the paraffin wax characteristic mode at 1400-1515 cm^{-1} (red color code) to the $\nu_1(PO_4^{-3})$ stretching at 960 cm^{-1} (green color code), b) the type-B carbonate stretching peak at 1070 cm^{-1} (red color

code) to the $\nu_1(PO_4^{-3})$ vibrational mode (green color code), and c) the collagen amide I band at 1667 cm^{-1} (red color code) to the $\nu_1(PO_4^{-3})$ vibrational mode (green color code). These maps indicate a small amount of phosphate in the *periosteum* of the tibiotarsi and none in the *bone marrow cavity*.

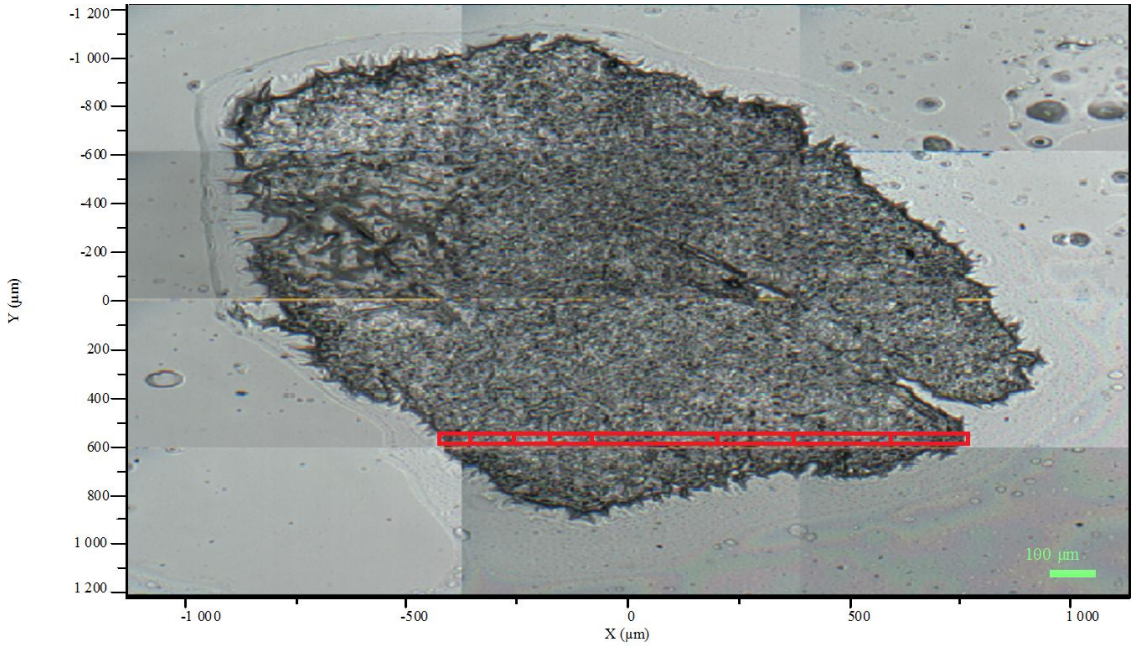

Figure 3.7: Optical image of the no injection control bone sample recorded using the 10x objective of the confocal Raman microscope. The outlined area in red indicates where the Raman mapping was performed.

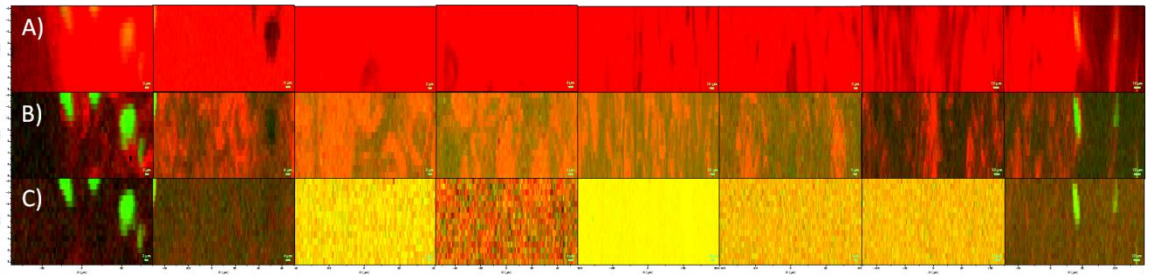

Figure 3.8: Raman mapping images generated for the no injection control bone sample by comparing A) the paraffin deformations (1400-1515 cm^{-1}, red) to the $\nu_1(PO_4^{3-})$ stretching band (960 cm^{-1}, green), B) the type B carbonate stretching mode (1070 cm^{-1}, red) to the $\nu_1(PO_4^{3-})$ vibrational mode (960 cm^{-1}, green), and C) the collagen amide I peak (1667 cm^{-1}, red) to the $\nu_1(PO_4^{3-})$ (960 cm^{-1}, green) vibrational mode.

Figure 3.9 shows the optical image (100x objective) of the PBS control bone sample. The red rectangle indicates the Raman mapped area. The Raman maps of the

PBS control sample are illustrated in Figure 3.10. These maps are created by comparing a) the paraffin wax deformations at 1400-1515 cm^{-1}(red color code) to the $\nu_1(PO_4^{-3})$ vibrational mode at 960 cm^{-1} (green color code), b) the type-B carbonate stretching mode at 1070 cm^{-1} (red color code) to the $\nu_1(PO_4^{-3})$ stretching band (green color code), and c) the collagen amide I peak at 1667 cm^{-1} (red color code) to $\nu_1(PO_4^{-3})$ vibrational mode (green color code). The Raman maps indicate increased amount of phosphate within the *periosteum* and *bone marrow cavity*.

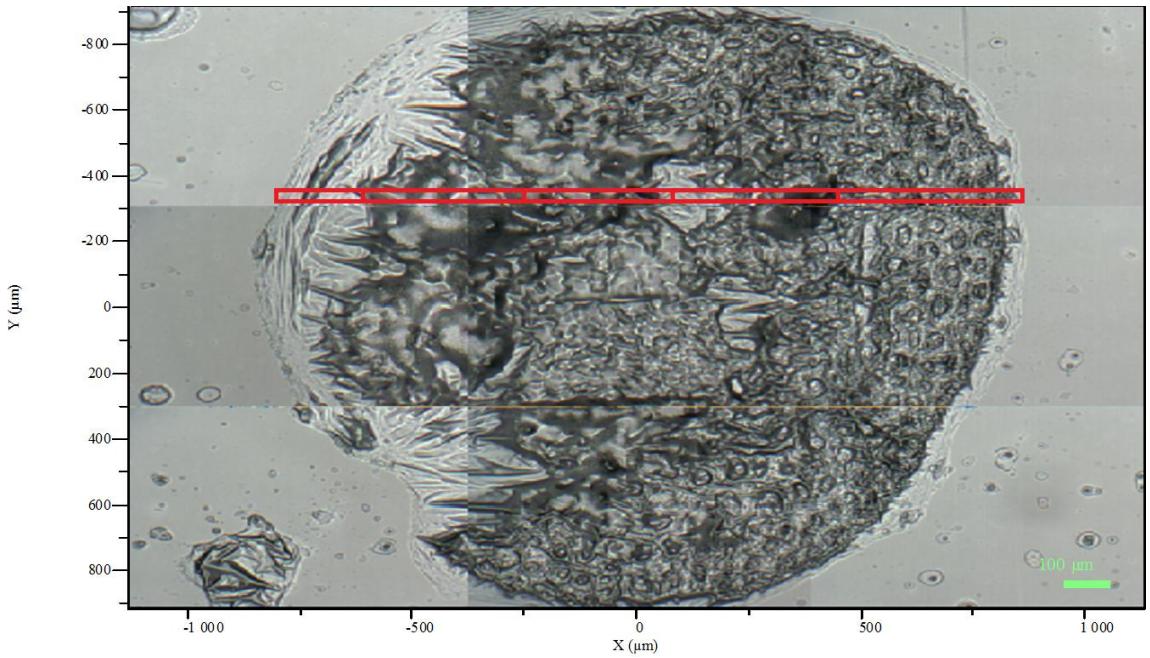

Figure 3.9: Optical image of the phosphate buffer solution control bone sample recorded using the 10x objective of the confocal Raman microscope. The outlined area in red indicates tha area of Raman mapping.

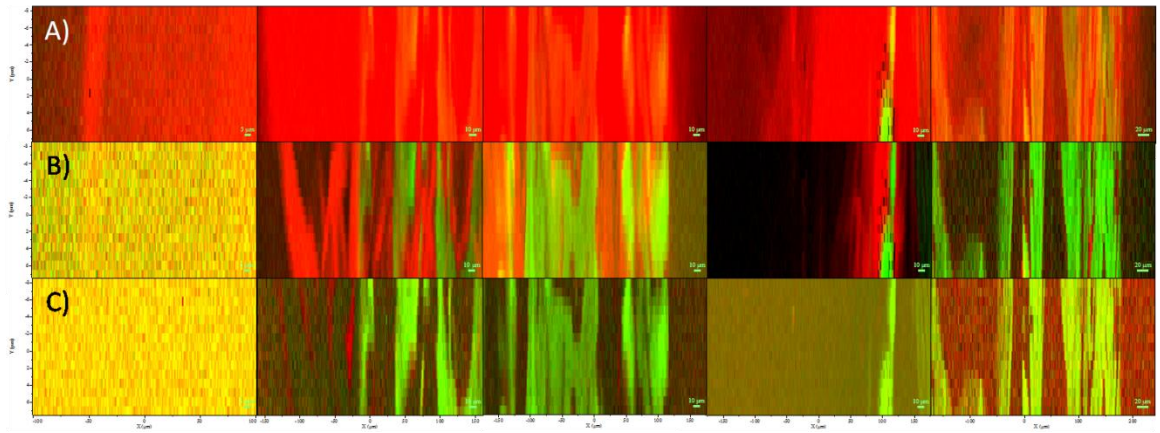

Figure 3.10: Raman mapping images generated for the phosphate buffer solution control bone sample by comparing A) the paraffin deformations (1400-1515 cm^{-1}, red) to the $\nu_1(PO_4^{3-})$ stretching band (960 cm^{-1}, green), B) the type B carbonate stretching mode (1070 cm^{-1}, red) to the $\nu_1(PO_4^{3-})$ vibrational mode (960 cm^{-1}, green), and C) the collagen amide I peak (1667 cm^{-1}, red) to the $\nu_1(PO_4^{3-})$ (960 cm^{-1}, green) vibrational mode.

Figure 3.11 shows the optical image (100x objective) of the 1.00 ppm Pt treatment bone sample. The red inset delimits the Raman mapped area. The corresponding Raman maps are inserted in Figure 3.12. The Raman maps are created by comparing a) the paraffin wax deformations at 1400-1515 cm^{-1}(red color code) to the $\nu_1(PO_4^{-3})$ vibrational mode at 960 cm^{-1} (green color code), b) the type-B carbonate stretching mode at 1070 cm^{-1} (red color code) to the $\nu_1(PO_4^{-3})$ stretching band (green color code), and c) the collagen amide I peak at 1667 cm^{-1} (red color code) to $\nu_1(PO_4^{-3})$ vibrational mode (green color code). The Raman maps indicate an increased amount of phosphate in only the *periosteum*.

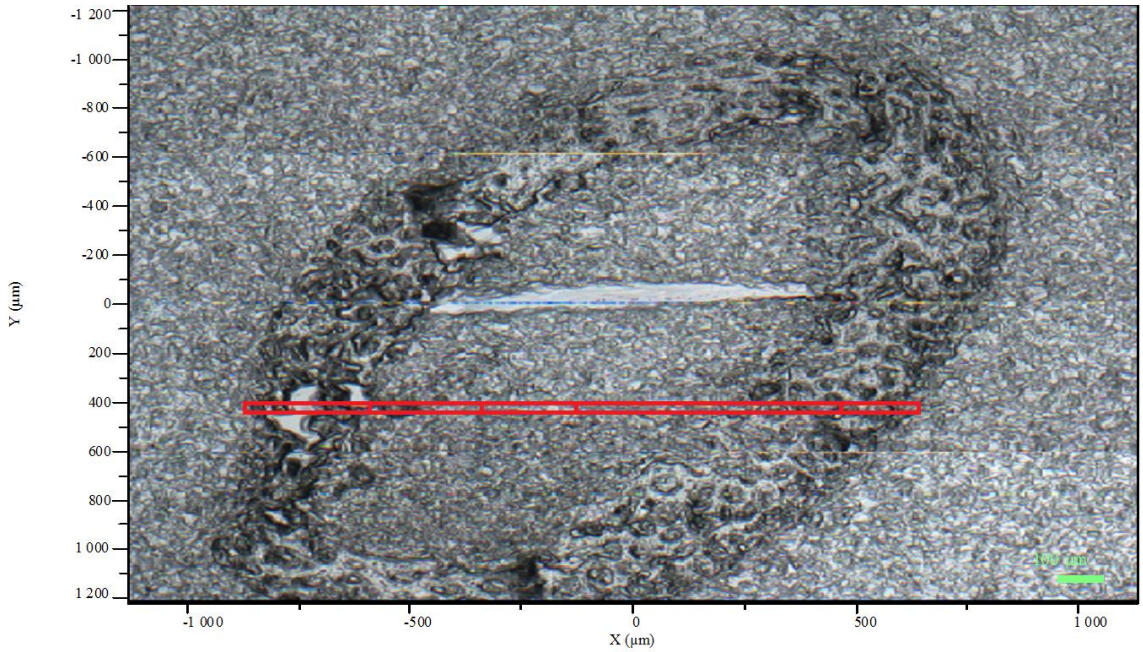

Figure 3.11: Optical image of the 1.0 ppm Pt treatment bone sample recorded using the 10x objective of the confocal Raman microscope. The area outlined in red indicates the area of Raman mapping.

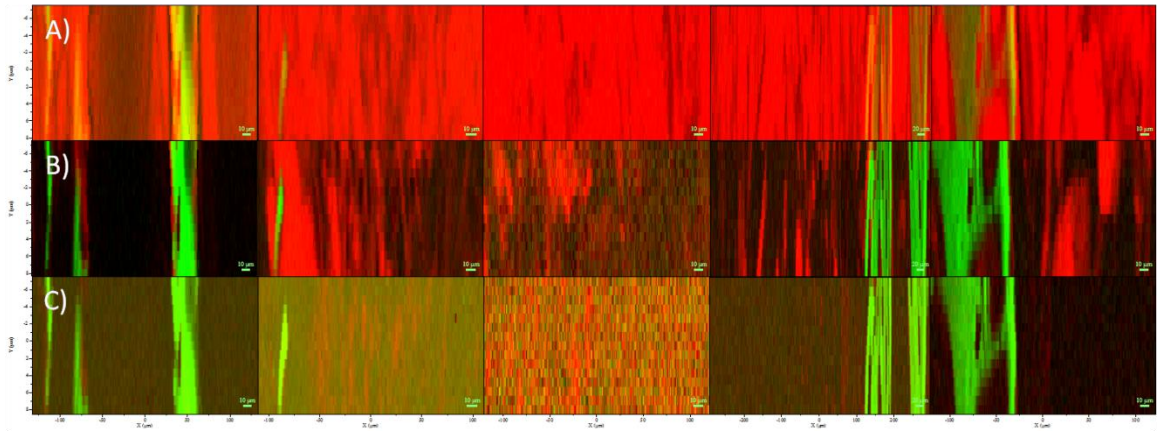

Figure 3.12: Raman mapping images generated for the 1.00 ppm Pt treatment bone sample by comparing A) the paraffin deformations (1400-1515 cm^{-1}, red) to the $\nu_1(PO_4^{3-})$ stretching band (960 cm^{-1}, green), B) the type B carbonate stretching mode (1070 cm^{-1}, red) to the $\nu_1(PO_4^{3-})$ vibrational mode (960 cm^{-1}, green), and C) the collagen amide I peak (1667 cm^{-1}, red) to the $\nu_1(PO_4^{3-})$ (960 cm^{-1}, green) vibrational mode.

Figure 3.13 shows the optical image (100x objective) of the 1 ppm Rh treatment bone sample and the Raman mapped area (marked with a red rectangle). A closer examination of the optical image reveals an unclean cut of the sample and confirms the softness of the bone tissue that was experienced during the microtome cutting process.

The corresponding Raman maps are inserted in Figure 3.14. The Raman maps are created by comparing a) the paraffin wax deformations at 1400-1515 cm^{-1}(red color code) to the $\nu_1(PO_4^{-3})$ vibrational mode at 960 cm^{-1} (green color code), b) the type-B carbonate stretching mode at 1070 cm^{-1} (red color code) to the $\nu_1(PO_4^{-3})$ stretching band (green color code), and c) the collagen amide I peak at 1667 cm^{-1} (red color code) to $\nu_1(PO_4^{-3})$ vibrational mode (green color code). The Raman maps indicate an increased amount of phosphate only within the *periosteum*.

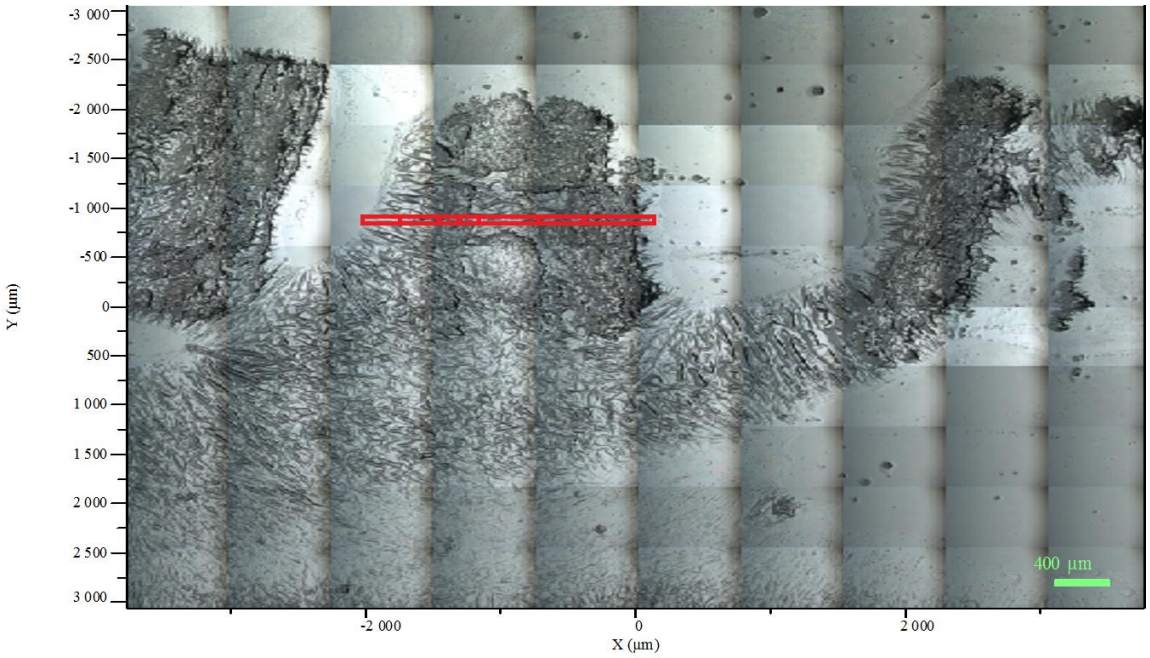

Figure 3.13: Optical image of the 1.0 ppm Rh treatment bone sample recorded using the 10x objective of the confocal Raman microscope. The outlined area in red indicates the area of Raman mapping.

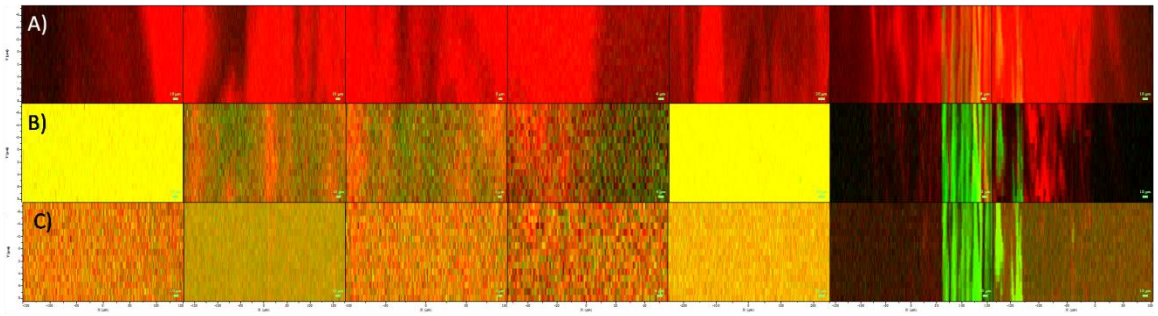

Figure 3.14: Raman mapping images generated for the 1.00 ppm Rh treatment bone sample by comparing A) the paraffin deformations (1400-1515 cm^{-1}, red) to the $\nu_1(PO_4^{3-})$ stretching band (960 cm^{-1}, green), B) the type B carbonate stretching mode (1070 cm^{-1}, red) to the $\nu_1(PO_4^{3-})$ vibrational mode (960 cm^{-1}, green), and C) the collagen amide I peak (1667 cm^{-1}, red) to the $\nu_1(PO_4^{3-})$ (960 cm^{-1}, green) vibrational mode.

Figure 3.15 demonstrates the presence of an area of high mineral content in the 1 ppm Rh treatment bone sample. The optical image A) of this area shows abnormal morphology for the Rh treated tissue in comparison to the control sample. The Raman map B) confirms the existence of an abnormal highly crystallized area in the same location. The Raman spectrum C) demonstrates the "green" region of the Raman map has an unusually high content of calcium phosphate. The Raman spectrum D) shows that the red section of the Raman map is mainly made off paraffin wax.

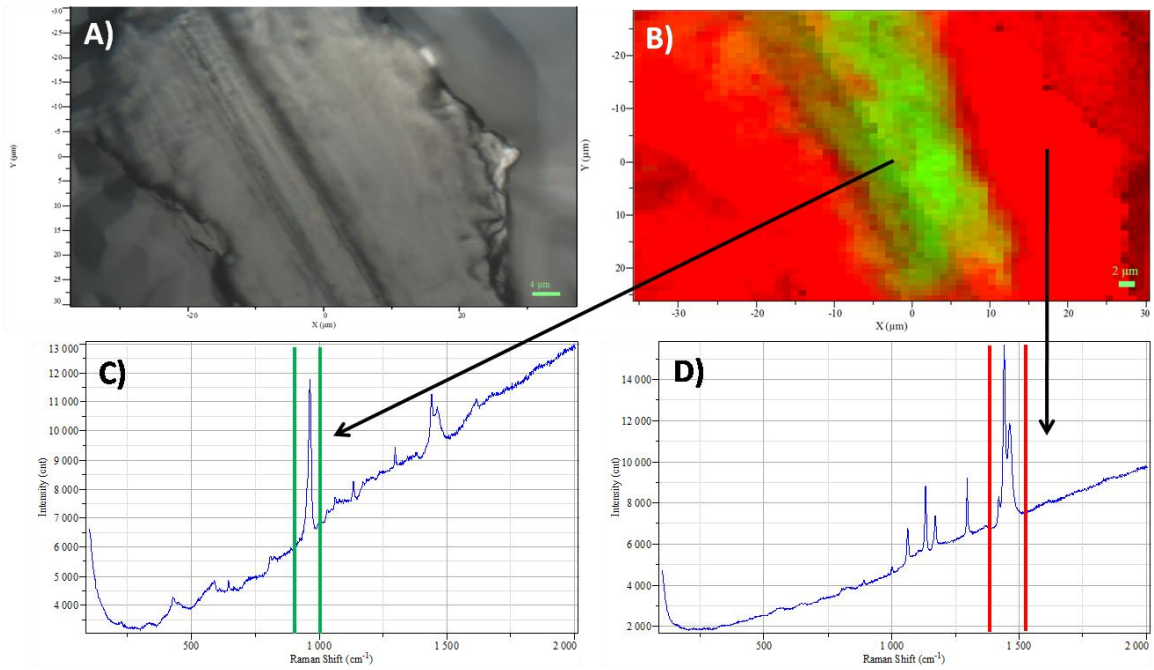

Figure 3.15: An area of an unusually high phosphate content found in the 1 ppm Rh treatment bone sample. A) Optical image recorded using the 100x objective of the confocal Raman microscope, B) Raman map (paraffin deformations are marked with red and the $\nu_1(PO_4^{3-})$ band is color coded in green), and C) the Raman spectrum of the high phosphate area D) the Raman spectrum of the paraffin area.

Figure 3.16 shows the optical image (100x objective) of the 1 ppm Pd treatment bone sample. The bone tissue section marked in red delimits the area studied using the Raman mapping feature. The corresponding Raman maps are inserted in Figure 3.17. The Raman maps are created by comparing a) the paraffin wax deformations at 1400-1515 cm^{-1} (red color code) to the $\nu_1(PO_4^{-3})$ vibrational mode at 960 cm^{-1} (green color code), b) the type-B carbonate stretching mode at 1070 cm^{-1} (red color code) to the $\nu_1(PO_4^{-3})$ stretching band (green color code), and c) the collagen amide I peak at 1667 cm^{-1} (red color code) to $\nu_1(PO_4^{-3})$ vibrational mode (green color code). The Raman maps indicate an increased amount of phosphate within the *periosteum*.

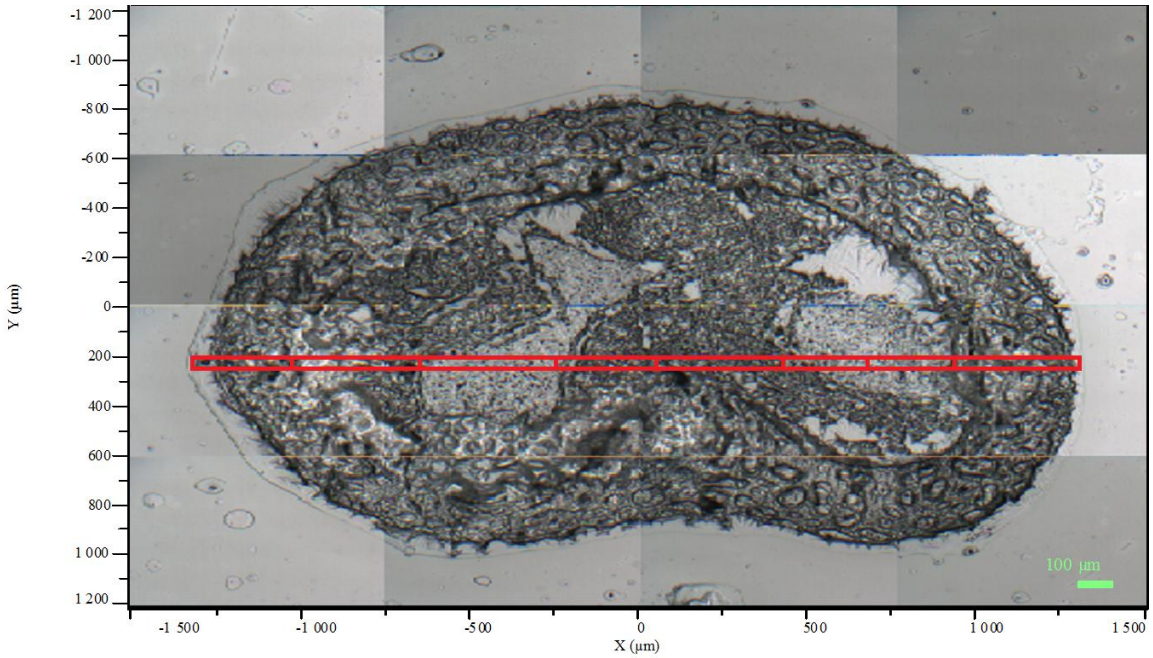

Figure 3.16: Optical image of the 1.0 ppm Pd treatment bone sample recorded using the 10x objective of the confocal Raman microscope. The outlined area in red indicates the area of Raman mapping.

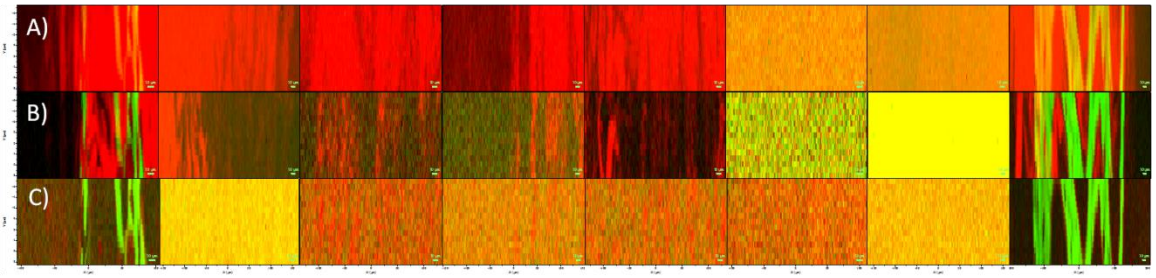

Figure 3.17: Raman mapping images generated for the 1.0 ppm Pd treatment bone sample by comparing A) the paraffin deformations (1400-1515 cm^{-1}, red) to the $\nu_1(PO_4^{3-})$ stretching band (960 cm^{-1}, green), B) the type B carbonate stretching mode (1070 cm^{-1}, red) to the $\nu_1(PO_4^{3-})$ vibrational mode (960 cm^{-1}, green), and C) the collagen amide I peak (1667 cm^{-1}, red) to the $\nu_1(PO_4^{3-})$ (960 cm^{-1}, green) vibrational mode.

Figure 3.18 shows the optical image (100x objective) of the PGM mixture treatment bone sample and the Raman mapped area (marked with a red rectangle). A closer examination of the optical image shows irregularities at the outer edges of the bone which were not detected in the control sample without an injection. Furthermore, this particular bone sample does not seem to have a bone marrow cavity. The corresponding Raman maps are inserted in Figure 3.19. The Raman maps are created by comparing a)

the paraffin wax deformations at 1400-1515 cm^{-1}(red color code) to the $\nu_1(PO_4^{-3})$ vibrational mode at 960 cm^{-1} (green color code), b) the type-B carbonate stretching mode at 1070 cm^{-1} (red color code) to the $\nu_1(PO_4^{-3})$ stretching band (green color code), and c) the collagen amide I peak at 1667 cm^{-1} (red color code) to $\nu_1(PO_4^{-3})$ vibrational mode (green color code). The Raman maps indicate an increased amount of phosphate within the *periosteum* and the *bone marrow cavity*.

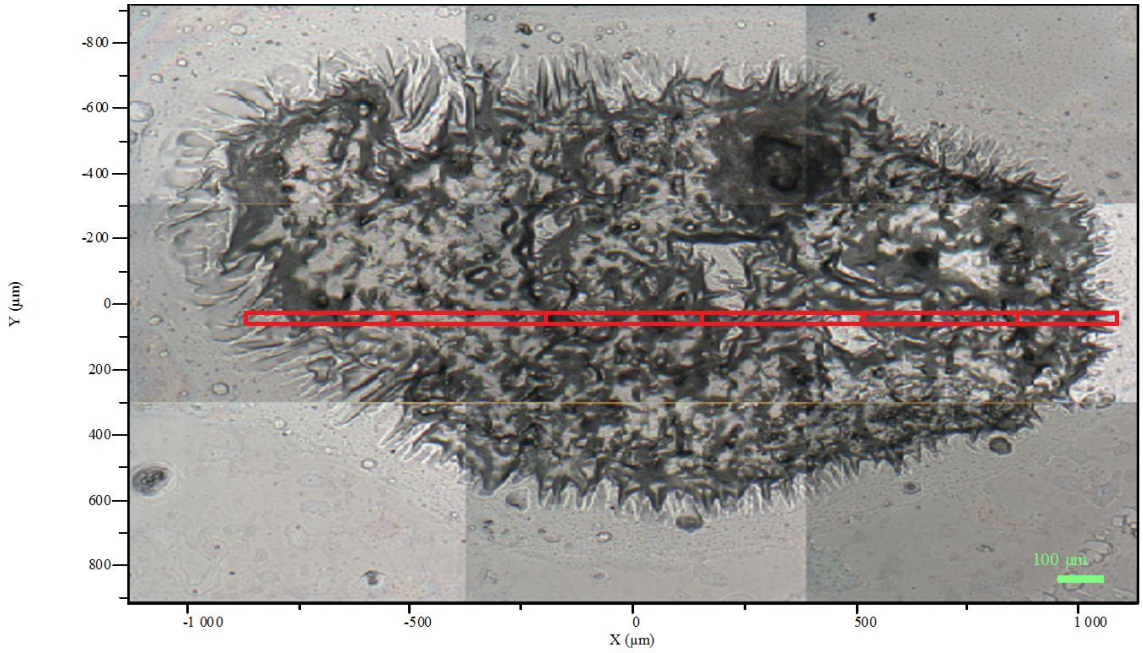

Figure 3.18: Optical image of the 1.0 PGM mixture treatment bone sample recorded using the 10x objective of the confocal Raman microscope. The outlined area in red indicates the area of Raman mapping.

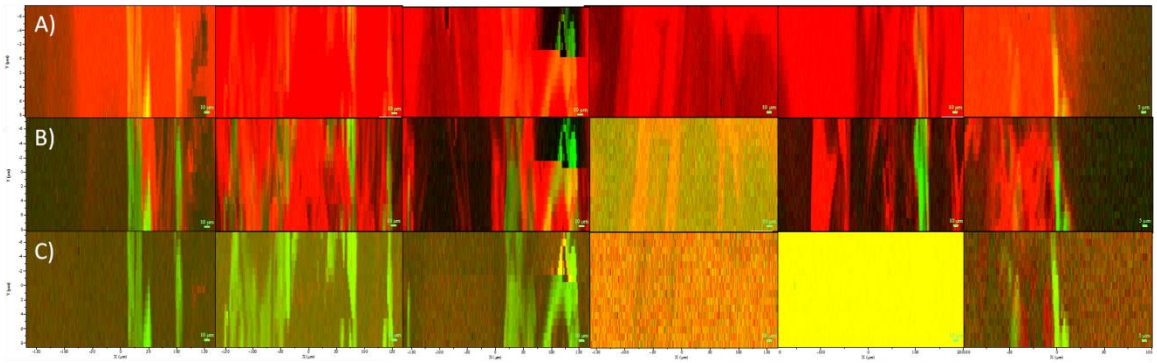

Figure 3.19: Optical image of the 1.0 ppm PGM mixture treatment bone sample recorded using the 10x objective of the confocal Raman microscope. The outlined area in red indicates where the Raman mapping was performed.

The Raman data also revealed information about: a) the age of mineral crystals (carbonate content), b) degree of mineralization of the collagen matrix, and c) mineral crystallinity. The age of the mineral crystals was determined from the ratio of relative intensities of the $\nu_1(CO_3^{2-})$ band at 1070 cm^{-1} compared to the $\nu_1(PO_4^{3-})$ band at 960 cm^{-1}. This value decreases when exposed to the 1.0 ppm Pd and Rh treatments, increases with the 1.0 PGMs treatment, and stays the same with the 1.0 ppm Pt and PBS treatments when compared to the control. The degree of mineralization of the collagen matrix values were calculated from the integrated areas of the $\nu_1(PO_4^{3-})$ band at 960 cm^{-1} to the α-amide I vibrational mode at 1670 cm^{-1}. This value decreases with the 1.0 ppm Pt, and stays the same (due to very large uncertainties) for all other treatments when compared to the control. The last value that was determined was the mineral crystallinity which is directly related to the full width at half maximum (FWHM) of the $\nu_1(PO_4^{3-})$ band at 960 cm^{-1}. This value statistically does not change due to the metal treatments. These caluclated values are found in Table 3.2

Table 3.2: Calculated values for the age of mineral crystals, degree of mineralization of the collagen matrix, and mineral crystallinity from eight micro-Raman spectra collected in areas of interest for each treatment.

	Age of Mineral Crystals	**Degree of Mineralization of the Collagen Matrix**	**Mineral Crystallinity (cm^{-1})**
Control	0.52 ± 0.28	3.4 ± 1.0	12.0 ±0.9
PBS	1.7 ± 1.4	4.7 ± 2.2	13.7 ± 1.8
Pt	1.8 ± 0.9	1.0 ± 0.7	12.3 ± 0.8
Rh	0.06 ± 0.03	2.3 ± 1.3	12.1 ± 0.7
Pd	0.005 ± 0.001	6.4 ± 5.0	12.4 ± 0.59
PGMs	2.3 ± 0.9	4. 5 ± 2.1	13.5 ± 1.4

III. X-RAY FLUORESCENCE DATA

The following gross observations were made in relation to the mechanical properties of the tibiotarsi during longitudinal sectioning for X-Ray fluorescence measurements:

a) For all Pt treatments of 0.1 ppm, the tibiotarsus length was longer in comparison with the control sample. The following values represent the percent increase in length compared to the no injection sample: 0.1 ppm – 25.56%, 1.0 ppm – 11.28%, 5.0 ppm – 9.78%, and 10.0 ppm – 4.17%. The exception to this trend was the 10.0 ppm Pt (dead) sample, which decreased in length compared to the control (7.78% decrease). For Pt treatments higher than 0.1 ppm, the tissue specimens were noticeably softer and a clean cut was difficult to obtain.

b) For all Rh treatments, tibiotarsi were longer than the corresponding control specimens. The following values represent the percent increase in length compared to the no injection sample: 0.1 ppm – 26.50%, 1.0 ppm – 23.33%, 5.0 ppm – 9.83%, and 10.0 ppm – 18.33%. For Rh exposures of 0.1 ppm and 1.0 ppm, tibiotarsi could be easily sectioned, while for Rh exposures of 5.0 and 10.0 ppm, it was difficult to obtain a clean cut due to softer bone tissue.

c) For the 1.0 ppm Pd treatment, the tibiotarsi had approximately the same length as in the control sample, whereas the 5.0 ppm Pd treatment caused a 13.50% increase in tibiotarsus length. The two bone samples were harder, which allowed for easier sectioning.

d) For the PGM mixture concentrations, tibiotarsi were longer (0.1 ppm – 22.94% and 1.0 ppm – 19.72%) and thinner in comparison to the control.

Tibiotarsus lengths are found in Table 3.3. These lengths were determined from the X-Ray fluorescence optical images by using a ruler and the provided scale bar. It should be noted that the high standard deviation for the 5.0 ppm Pt treatment was due to inaccurate measurements caused by the light reflecting on the X-Ray film.

Table 3.3: Lengths of the chick embryo tibiotarsi

Treatment	Length (mm)	% Difference from no injection
No injection	18.00 ± 0.48	-
0.1 ppm Pt	22.60 ± 0.53	25.56 ± 2.35
1.0 ppm Pt	20.03 ± 0.53	11.28 ± 2.65
5.0 ppm Pt	19.76 ± 1.46	9.78 ± 7.39
10.0 ppm Pt	18.75 ± 0.36	4.17 ± 1.92
10.0 ppm Pt (dead)	16.60 ± 0.44	7.78 ± 2.65
0.1 ppm Rh	22.77 ± 0.61	26.50 ± 2.68
1.0 ppm Rh	22.20 ± 0.17	23.33 ± 0.77
5.0 ppm Rh	19.77 ± 0.12	9.83 ± 0.61
10.0 ppm Rh	21.30 ± 0.10	18.33 ± 0.47
1.0 ppm Pd	17.68 ± 0.33	2.06 ± 1.87
5.0 ppm Pd	20.43 ± 0.21	13.50 ± 1.03
0.1 ppm PGMs	22.13 ± 0.06	22.94 ± 0.27
1.0 ppm PGMs	21.55 ± 0.51	19.72 ± 2.37

Calcium, one of the major elements in bone, was examined in relation to the PGM exposure level. The X-Ray fluorescence data obtained on the longitudinal sections revealed that the distribution of calcium in developing chick tibiotarsus was influenced by the PGM exposure.

a) For the Pt treatment (Figure 3.20), calcium content seems to decline steadily with increasing metal concentration except for the 5.0 ppm Pt treatment, where the calcium deposition increased. The most dramatic changes were observed for the bone marrow cavities where almost no calcium was detected. The chick embryo marked as “dead” in Figure 3.21 was found to be undeveloped at the time of harvesting. It can be easily

noticed that calcium content is increased in the distal end of the tibiotarsus outer and inner sections.

b) For the Rh treatments (Figure 3.21), onset of calcification was detected at an exposure level of 0.1 ppm, in particular at the distal end of the *periosteum* (i.e., the external dense membrane composed of fibrous connective tissue closely wrapping the bone marrow). Small calcium depositions were also found in the bone marrow cavities for the 0.1 ppm treatment. For Rh treatments of 1.0 ppm and higher, the calcium content steadily decreased in the inner and outer tibiotarsus portions with the increase in Rh concentration. The most significant changes were observed within the bone marrow cavities, which were depleted of calcium.

c) For the Pd treatment of 1.0 ppm (Figure 3.22), larger calcium deposits were recorded in *periosteum* in comparison with the control tibiotarsus sections. Bone marrow cavities seemed to have a slightly higher content of calcium than the control sample. For the Pd treatment of 5.0 ppm, a similar slight decrease in the calcium content was noticed in comparison with the control sections. Unfortunately, for the 0.1 and 10.0 ppm Pd treatments there were not enough samples to be analyzed via X-ray fluorescence. This was due to the smaller amount of viable chick embryo eggs for these treatments.

d) For the PGM mixture treatment of 0.1 ppm (Figure 3.23), a larger calcium deposition was detected in the distal *periosteum* and central *bone marrow cavities* of the tibiotarsus in comparison with the control sample. A similar calcium distribution pattern was noticed for the PGM mixture treatment of 1.0 ppm, but of lower intensity.

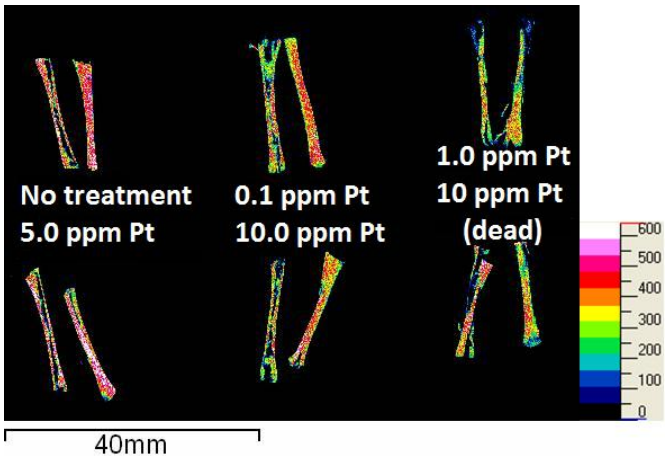

Figure 3.20 X-Ray fluorescence image of the entire Pt treated bone samples showing the amount of calcium present. The magnitudes of the scale bar were increased ten-fold in comparison to the following figures. This accounts for the differences seen in the control sample. These measurements will be repeated. The inner portion of the tibiotarsi is located on the left side for each treatment.

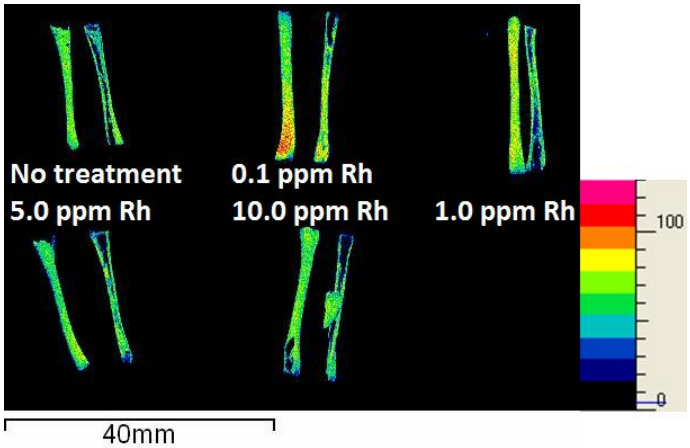

Figure 3.21: X-Ray fluorescence image of the entire Rh treated bone samples showing the amount of calcium present. The inner portion of the tibiotarsi is located on the right side for each treatment.

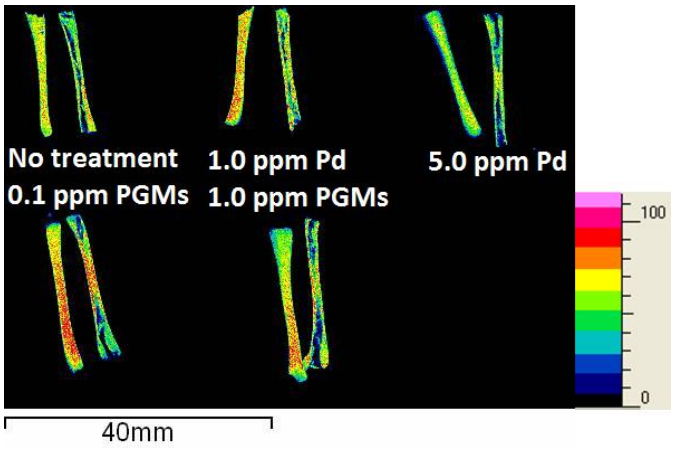

Figure 3.22: X-Ray fluorescence image of 1.0 ppm Pd, 5.0 ppm Pd, 0.1 ppm PGMs, and 1.0 ppm PGMs treated bone samples showing the amount of calcium present. The inner portion of the tibiotarsi is located on the right side for each treatment.

IV. ATOMIC ABSORPTION DATA

The average amount of calcium in the cartilage/bone samples was determined via FAAS. The instrument was calibrated using seven known standards of 0.1, 0.2, 0.5, 1.0, 2.0, and 4 ppm of calcium (Figure 3.23). One no injection control tibiotarsi was analyzed and two metal treatment samples were analyzed. Equation 3.3 was used to determine the average calcium content (µg/g) within the sample, where *C* is the raw average calcium content (mg/L), *V* is the volume (mL) of the undiluted original sample, $d_n f_n$ is the dilution factor (put the signal from the sample on scale and within the calibration curve produced), and *W* is the weight of the original dry sample in grams.

$$\frac{\mu g}{g} = \frac{CVd_nf_n}{W} \tag{3.3}$$

This value is converted to percent calcium. The percent calcium determined for the control sample was16.1%. Table 3.4 shows the percent calcium calculations for the PGM treatments. The percent calcium values were significantly decreased for the 1.0 ppm Pt and PGMs mixture treatment samples whereas the 1.0 ppm Pd treatment showed a drastic

increase in comparison to the no injection control. The 1.0 ppm Rh treatment only increased by 1.2%.

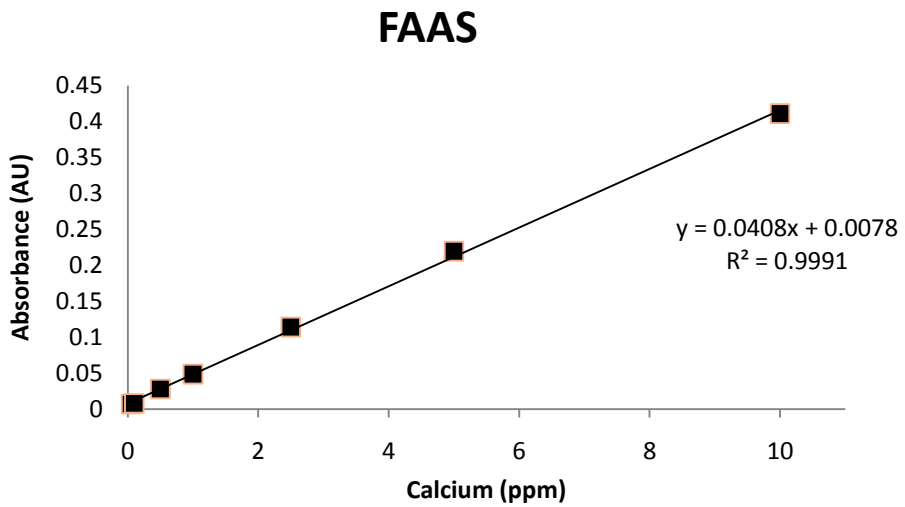

Figure 3.23: Flame atomic absorption spectroscopy calibration curve constructed using seven calcium standards of 0.1, 0.2, 0.5, 1.0, 2.0, and 4 ppm.

Table 3.4: Percent calcium content found in all 1.0 ppm PGM treatments.

Sample Description	Average % Calcium
Control	16.1 ± 0.2
Pt 1.0 ppm	8.88 ± 0.29
Rh 1.0 ppm	17.8 ± 0.3
Pd 1.0 ppm	24.3 ± 0.4
PGMs 1.0 ppm	13.9 ± 0.1

4. DISCUSSION

I. HISTOPATHOLOGY

Gross Pathology

Initial gross pathological observations of developing chick embryos exposed to PGMs were devastating. Striking abnormalities such as brain protrusion from the skull (figure 3.1A) and formation of abdominal organs outside of the body cavity (figure 3.1B) were witnessed for all PGM treatments higher than 1.0 ppm. These deformities are clearly the result of severe bone malformations. A properly formed skull should withstand the pressure created by a developing brain and its surrounding fluids. However, if the skeleton does not present the expected mechanical properties (i.e., hardness, elasticity, roughness, and strength) and morphology (i.e., age of mineral crystals, degree of mineralization of the collagen matrix, and mineral crystallinity), it will not withstand bending, stretching, twisting, and compression. Therefore, the brain easily splits the top of the skull with little or no resistance. Similarly, if the development of rib cage is hindered due to the PGM exposure, a lack of internalization of abdominal organs will be experienced. Ribs develop normally in the membrane during embryonic development at the end of day 6, become cartilaginous by day 7.5, and ossify by day 12. The ossification process of the rib cage was not normal or completed in the chick embryos exposed to PGMs over 1 ppm.

Histology

Exposure to PGMs had adverse effects upon the development of chondrocyte cells in cartilage. Histological analysis revealed a decrease in the chondrocyte diameters in all PGM treatments. Knowing that chondrocytes have an essential role in the synthesis of various matrix constituents, an abnormal cartilage development is expected due to these developmental changes. This histological observation further supports the gross pathological observations. More studies are necessary provide a detailed mechanism for the decreased chondrocyte diameters.

II. RAMAN SPECTROSCOPY

The micro-Raman spectrum of the paraffin wax control (Figure 3.4) was first collected to determine the contributions of the embedding material to the spectra of all tibiotarsi. Two micro-Raman spectra obtained from the no injection control and 1.0 ppm PGM mixture sample were inserted in Figure 3.5 and 3.6 for comparison reasons. A detailed vibrational assignment was prepared in Table 3.6 for each significant band in the micro-Raman spectra according to literature. This allowed for the identification of the paraffin wax characteristic vibrational modes (271, 418, 528, 645, 715, 808, 1003, 1033, 1064, 1137, 1174, 1299, 1372, 1420, 1442, 1464, and 1613 cm^{-1}).

During initial measurements, the paraffin embedding material at 1400-1515 cm^{-1} was compared to the $\nu_1(PO_4^{3-})$ band at 960 cm^{-1} to identify the regions of possible higher mineral content. Calcium mineral in hydroxyapetite is indirectly determined in the Raman spectrum based on the phosphate vibrational mode. As expected, regions of unusually high calcium inclusions were sporadically found in the tibiotarsus cross-sections for all PGM treatments. The no injection control sample (figure 3.8) exhibited a

few areas of high crystallization at the outer edges of the bone. However, this was expected because those *periosteum* regions usually contain ossified bone. In contrast to the no injection control sample, the PBS treatment (figure 3.10) led to the formation of abnormal calcium inclusions within the *bone marrow cavity*. In all three 1.0 ppm individual metal treatments (i.e., Pt, Rh, and Pd), areas of unusual high mineral content were found within the outer edges of the bone (figures 3.12, 3.14 and 3.17). These areas were of increased size and quantity in comparison to the no injection control. The 1.0 ppm PGM mixture treatment caused an increase in mineral content throughout the whole bone cross-section (figure 3.19). However, the observed abnormal increase in mineral content due to the PBS treatment, this may be causing a systematic increase in all the metal treatments.

According to Bellairs and Osmon, the precartilaginous precursors of tibiotarsus are formed by day five and ossification begins on day six.[12] The ossification process is completed by the 11th week after hatching.[12] Because the tibiotarsi are mostly composed of cartilage during development, nutrients and waste are transported through long range diffusion.[13] Therefore, the presence of abnormal calcium inclusions may inhibit the transport of essential nutrients, oxygen and waste through the matrix, and may cause blockages of the vasculatore system during the pre-hatching phase of chick development. Ultimately, these effects may lead to the observed skeletal deformities in the growing embryo exposed to PGMs.[13]

As shown in the Raman Data section (table 3.2), specific Raman band features are used to estimate: A) the age of mineral crystals, B) the degree of mineralization of the collagen matrix, and C) the mineral crystallinity.

a) The calculations for determining the age of mineral crystallinity revealed a drastic decrease in the Rh and Pd exposures but an increase in the PGMs mixture treatment. It is important to realize the age calculated due to the PBS exposure has an abnormally high uncertainty value. Because the PBS sample is another control, no definitive conclusion can be determined at this time due to this high uncertainty value.

b) The signal-to-noise ratio in the 1600-1700 cm^{-1} spectral region, characteristic to amide I collagen vibrational modes, was very low for the chosen Raman-mapping acquisition time of three seconds. This resulted in high uncertainties for the calculated inorganic versus organic matrix components ratio. Even with the low signal-to-noise ratio and the resulting high uncertainties, a small decrease in the degree of mineralization was established for the 1.0 ppm Pt treatment sample. As it will be shown later in the FAAS discussion section, the largest calcium mineral loss was detected for the 1.0 ppm Pt treatment. This calcium loss provides more evidence for the observed skeletal pathological changes. Point Raman measurements of longer acquisition times will be performed to re-evaluate the inorganic versus organic matrix ratios for the other metal treatments.

c) The changes estimated in mineral crystallinity for all metal treatments as compared to the no injection control sample is inconclusive at this time when accounting for the spatial resolution of the micro-Raman instrument for the 600 groove/mm holographic grating is 1.1 cm^{-1} and the calculated uncertainties that are within the same wavenumber range.

III. X-RAY FLUORESCENCE MICROSCOPY

X-Ray fluorescence images (figures 3.20 – 3.22) showed a significant redistribution of calcium within the chick embryo tibiotarsi as compared to the no injection control sample. Specifically, regions of unusual high calcium content were identified in the *periosteum* of tibiotarsi for all 1.0 ppm metal treatments including PGM mixture as well as in the *bone marrow cavity* for PGM mixture alone. These results confirm the calcium redistribution pattern revealed by the Raman-mapping observations for all 1.0 ppm treatments and controls (figures 3.8, 3.12, 3.14, 3.17. and 3.19).

IV. FLAME ATOMIC ABSORPTION SPECTROSCOPY

The FAAS measurements of tibiotarsi of chick embryos exposed to PGMs revealed a significant decrease in the average percent calcium with respect to the no injection control sample for the 1.0 ppm Pt and PGM treatments (Table 3.4). The largest percent calcium difference from the no injection control was determined to be 55.1% for the 1.0 ppm Pd treatment. This was followed by 44.8 % for the 1.0 ppm Pt, 13.7 % for the 1.0 ppm PGMs, and 10.6 % for 1.0 Rh treatment. The observed decrease in average calcium content is indicative of an overall loss in bone mineral density making the bone much weaker than it should be. In contrast, the increase in the average calcium content reveals older, more brittle bone in comparison to the control. It is now obvious that the presence of PGMs is directly correlated with the enormous loss and redistributions in bone mineral density and may explain the observed morphological and pathological changes in the chick skeleton (i.e., limb deformities, smaller chondrocyte cells, etc.). Unfortunately, an exact mechanism explaining these enormous losses in calcium is not known at this time.

V. CONCLUSIONS

The widespread use of PGMs raises concerns for potential adverse health effects in living organisms. It has been documented that PGMs are readily bioaccumulated into plant tissue, allowing for these metals to enter the food chain of animals and humans.[36,37] In this study, we examined the skeletal pathology of tibiotarsi in chick embryos exposed to platinum group metals by micro-Raman spectroscopy, X-ray fluorescence, and flame atomic absorption spectroscopy. This research has shown that exposure to PGMs is detrimental to chick embryo skeletal development. This observation was expected due to the small quantity of toxicity studies on PGMs present in literature.[1-10] Micro-Raman spectroscopy revealed the formation of abnormal calcium deposits within the cartilage matrix of chick embryo tibiotarsi for all 1.0 ppm metal treatments. X-ray fluorescence measurements confirmed the Raman data and calcium redistribution pattern observed within the *periosteum* and *bone marrow cavity* of tibiotarsi. Flame atomic absorption spectroscopy showed enormous decreases in the average percent calcium for all platinum group metal treatments, which further explains the observed limb deformities and decrease in chondrocyte cell diameter. Micro-Raman spectroscopy in combination with X-ray fluorescence spectroscopy and flame atomic absorption spectroscopy were successful analytical techniques for the investigation of chick embryo skeletal pathology. Because chick embryos are in the family of amniotes, the potential for similar effects to other animal species, including pregnant woment, may be possible.

VI. FUTURE ENDEAVORS

Further analysis should be continued in order to understand the toxicological effects of PGMs on the chick embryo animal model. Some scientific aims that are of interest for a future graduate student are:

1) To complete the micro-Raman spectroscopy and FAAS investigations on tibiotarsi for the other PGM exposure levels (0.1 ppm, 5.0 ppm, and 10.0 ppm), and to correlate these results with the already collected X-Ray fluorescence data and observed pathological changes.
2) To develop a computer software program for the complete analysis of the micro-Raman maps.
3) To observe and measure the PGMs bioaccumulation in the cartilage tissue of developing chick embryos.
4) To examine the effect of part per million versus molarity doses due to the differences in weights of the three metals.
5) To examine the relationship between the PGMs bioaccumulation and the induced morphological changes within the entire tibiotarsi.
6) To explore the possible mechanism(s) explaining the detrimental role of PGMs on the chick skeletal development.

REFERENCES

1. Klaassen, C.D. The Basic Science of Poisons, 5th Ed., McGraw-Hill, New York, 1996: 725-726
2. Gagnon, Z.E.; Newkirk, C.; Hicks, S. J. Environmental Science and Health Part A. 2006, 41: 397-414
3. Diehl, D.B.; Gagnon, Z.E. Water Air and Soil Pollution 2007, 184: 255-267
4. Alt, F., A. Bambauer, H. Hoppstock, B. Mergler, G. Toelg. Fresen Journal of Analytical Chemistry, 1993, 346(6): 693
5. Barbante, C., A. Veysseyre, C. Ferrari, K. Van de Velde, C. Morel, G. Capodaglio, P. Cescon, G. Scarponi, C. Boutron. Environmental Science and Technology, 2001, 35(5):835-839
6. Dubiella-Jackowska, A; *et al*. Critical Reviews in Analytical Chemistry. 2009, 39: 251-271
7. Rosenberg, B., L. VanCamp, J.E. Trosko, V.H. Mansour. Nature, 1969, 222:385-386
8. Gagnon, Z., M. Crocco, V. Porzio, C. Newkirk, N. Fitzgerald, J. Conetta. Proceedings of the 23rd Society of Environmental Toxicology and Chemistry, 2002, 491:107

9. Reeves, B., J. Zimmerman, C. Baker, V. Porzio, Z. Gagnon, C. Newkirk, J. Conetta. Proceedings of the 57th Annual Eastern Colleges Science Conference, 2003, B5

10. Osterauer, R.; Köhler, H.; Triebskorn, R. Aquatic Toxicology. 2010, 99: 100-107

11. World Health Organization. Air Quality Guidelines (2nd ed.), Chapter 6.11: Platinum. Retrieved March 13, 2006 from http://www.euro.who.int/document/aiq/6_11platinum.pdf, 2000

12. Bellairs, R., Osmond, M. The Atlas of Chick Development. Academic Press. 1998; Ch.10

13. Cormack, D. H. Dense Connective Tissue, Cartilage, Bone, and Joints in Essential Histology, 2nd Ed. Lippincott Williams and Wilkins. 2001.

14. Robey, P.G.; Boskey, A.L. Primer on the Metabolic Bone Diseases and Disorders of Mineral Metabolism, 6th Ed. American Society for Bone and Mineral Research. 2006; Ch. 3: 12-19

15. Cogburn, L.; Porter, T.; Duclos, M.; Simon, J.; Burgess, S.; Cheng, H.; Dodgson, J.; Burnside, Journal of Poultry Science. 2007, 86: 2059-2094

16. Stern C.D. Developmental Cell. 2005; 8: 9-17.

17. NIH Revitalization Act of 1993. Pub. L. no. 103-43. Sec. 205 (1993)

18. Hanig J.; Aiello E.; Seifter J. European Journal of Pharmacology. 1970; 12(2):180-182.

19. Hamburger, V.; Hamilton, H. Journal of Morphology. 1951; 88: 49-92.

20. Silbey, R.J.; Alberty, R.A.; Bawendi, M.G. Physical Chemistry, 4th Ed. John Wiley & Sons, Inc. Hoboken, NJ. 2005;Ch 13: p. 491-496.

21. Engel, Thomas. Quantum Chemistry and Spectroscopy. Pearson Education, Inc. Benjamin Cummings: San Francisco CA. 2006: Ch 8.

22. Akkus, O. *et al*, M. B. Journal of Bone and Mineral Research. 2003; 18(6): 1012-1019

23. Penel, G., Delfosse, C., Descamps, M., Leroy, G. Bone 2005; 36: 893-901

24. Kubisz, L., Polomska, M. Spectrochimica Acta Part A 2006; 66: 616-625

25. Van Apeldoorn, A.A., Aksenov, Y., Stinger M., Hofland, I., de Bruijn, J.D., Koerten, H.K., Otto, C., Greve, J., Blitterswijk, C.A.. Journal of the Royal Society Interface. 2005; 2: 39-45

26. Faoláin, E; Hunter, M; Byrne, J; Kelehan, P; Lambkin, H; Byrne, H; Lyng, F. Journal of Histochemistry and Cytochemistry. 2005, 53: 121-129

27. Yeni, Y. N., Yerramshetty, J., Akkus, O., Pechey, C., Les, C. M. Calcified Tissue International. 2006; 78: 363-371

28. Zou, S., Hunag, J., Best, S., Bonfield, W. Journal of Materials Science-Materials in Medicine. 2005; 16: 1143-1148

29. Akkus, O., Adar, F., Schaffler, M. B. Bone 2004; 34: 443-453

30. HRE-3919A. Horiba, Ltd. Kyoto, Japan

31. L'vov, B.V. Journal of Analytical Chemistry. 2005; 60(4): 434-446

32. Bettancort, J. Histology Laboratory Manual. Marist College, 2008: 15-26

33. LabRam 800 User Manual. Horiba Jobin Yvon, Inc. Edison NJ.

34. Atkinson, A; Jain, SC. Journal of Raman Spectroscopy. 1999; 30: 885-891

35. Leszek, K; Polomska, M. Spectrochimica Acta Part A. 2006; 66: 616-625

36. Ravindra, K., László, B., Van Grieken, R. Science of the Total Environment. 2004; 318:1-43

37. Gomez, B., Palacios, M.A., Gomez, M., Sanchez, J.L., Morrison, G., Rauch, S., McLeod, C., Ma, R., Caroli, S., Alimonti, A., Petrucci, E., Bocca, B., Schramel, P., Zischka, M., Petterson, C., Wass, U. Science of the Total Environment. 2002; 299 (1-3):1-9